micromachines

Review

Sn-Based Perovskite Solar Cells towards High Stability and Performance

Wafa' Ayaydah , Eman Raddad and Zafer Hawash *

Department of Physics, Birzeit University, Birzeit, Ramallah 71939, Palestine
* Correspondence: zhawash@birzeit.edu

Abstract: Recent years have witnessed rapid development in the field of tin-based perovskite solar cells (TPSCs) due to their environmental friendliness and tremendous potential in the photovoltaic field. Most of the high-performance PSCs are based on lead as the light-absorber material. However, the toxicity of lead and the commercialization raise concerns about potential health and environmental hazards. TPSCs can maintain all the optoelectronic properties of lead PSCs, as well as feature a favorable smaller bandgap. However, TPSCs tend to undergo rapid oxidation, crystallization, and charge recombination, which make it difficult to unlock the full potential of such perovskites. Here, we shed light on the most critical features and mechanisms affecting the growth, oxidation, crystallization, morphology, energy levels, stability, and performance of TPSCs. We also investigate the recent strategies, such as interfaces and bulk additives, built-in electric field, and alternative charge transport materials that are used to enhance the performance of the TPSCs. More importantly, we have summarized most of the recent best-performing lead-free and lead-mixed TPSCs. This review aims to help future research in TPSCs to produce highly stable and efficient solar cells.

Keywords: tin perovskites; stability; power conversion efficiency; crystallization; charge recombination

check for updates

Citation: Ayaydah, W.; Raddad, E.; Hawash, Z. Sn-Based Perovskite Solar Cells towards High Stability and Performance. *Micromachines* **2023**, *14*, 806. https://doi.org/10.3390/mi14040806

Academic Editors: Sadia Ameen and Jung Yong Kim

Received: 9 March 2023
Revised: 29 March 2023
Accepted: 30 March 2023
Published: 31 March 2023

1. Introduction

Nowadays, perovskites solar cells (PSCs) are considered as one of the most promising clean and renewable energy technologies. PSCs have achieved a high power conversion energy (PCE) up to about 26% [1,2], making it one of the most compelling research fields. Additionally, PSCs have enormous potential and versatile applications starting from solar plants for daily use electricity up to being utilized in space applications due to their appealing properties (light weight, low cost, flexibility, high PCE, and radiation tolerance) [3]. The ideal crystal structure of perovskites is cubic and based on the formula ABX_3. The cation 'A' (organic or inorganic such as methylammonium (MA), formamidinium (FA), or Cs) occupies the vertices of the cubic lattice. The 'X' anions (oxygen or halogen (Cl^-, Br^-, or I^-)) are located at the faces. The 'B' cation (Cu^{+2}, Sn^{+2}, or Pb^{+2}) occupies the octahedral site. Perovskites containing halides were introduced for the first time in 1978 [4]. However, the first PSC with halides was reported in 2009 [5].

Currently, all high-performance PSCs contain Pb in the light absorber since it is proven to provide superior opto-electronic properties, such as high absorption coefficient [6] and excellent transport capability [7]. However, lead toxicity and the correlated need for large-scale commercialization of PSCs raise concerns about the hazards that Pb may cause to humans and the environment [8]. Pb can rapidly enter the human bodies through inhalation, causing dangerous effects on the organs of the body even a on molecular level [9]. Therefore, there is an urgent need to replace the toxic lead with elements that have less toxicity or none. Some of the suggested alternatives are Sn, Sb, Bi, or Ge [10–15]. Between these fundamental elements, Sn presents itself as one of the most promising options [16–22]. Sn is a group 14 element in the periodic table, and it has a similar ionic radius (115 pm) to Pb (119 pm), allowing for $ASnX_3$ perovskites to develop [19]. In comparison to the Pb-based perovskites, Sn-based perovskites exhibit similar superior optoelectronic properties, with a narrower bandgap of about 1.3 eV [23], high charge mobilities of about 600 $cm^2.V^{-1}s^{-1}$ [24], long carrier diffusion and lifetime [25], and high absorption coefficients (>10^{-4} cm^{-1}) [26].

Based on the detailed balance limit, the evaluated value of the PCE of the Sn-based perovskite solar cells (TPSCs) is about 30% [27,28]. However, the PCE that is reported until now is much lower than that for Pb-based perovskites. The poor stability of Sn perovskites in a moist environment [29], as well as the presence of oxygen [30], under light irradiation [31], applied electric field [32], thermal stresses [33], and defects in the perovskite materials [34], all contribute to the often observed low PCE. Tin (i.e., Sn^{+2}) oxidizes fast to form Sn^{+4} due to its tendency to be more stable. It functions as a p-type dopant in the structure, resulting in an excessively high dark-carrier concentration and extremely high photo-carrier recombination [35–37]. It has low formation energies, which results in the creation of Sn vacancies, causing large amounts of self-doping in perovskite films and resulting in further non-radiative recombination losses [38]. Therefore, the performance and progress of the TPSCs is still behind the Pb-based PSCs and exhibiting significantly lower bioavailability.

In recent years, enormous progress and research on TPSCs have been reported and conducted. This review summarizes the most important aspects as well as the recent progress of TPSCs. The basic and most common device structure and the characteristics of each layer of TPCS are discussed and compared with those of Pb-based PCSs. The factors that are affecting the performance and stability of TPSCs, including additives (to precursor or at the interface), crystallization, strains, morphology, built-in electric field, charge extraction, energy levels, alternative charge transport materials, and solvents are presented and discussed.

2. Sn Perovskite Materials

2.1. High Conductivity and Metallic Behavior

A very important insight about the electronic properties of Sn-based perovskites goes back to the work reported by Yamada et al. [39] in 1990. They investigated a set of different $ASnI_3$ perovskites (A = K, NH_4, Rb, Cs, or MA). Both of the investigated Cs and MA -SnI_3 perovskites exhibited high conductivity at room temperature (Figure 1a), which was found to be in the range of 10^2–10^3 S cm^{-1} [39]. However, in the case of $CsSnI_3$, this conductivity that is similar to metallic materials was only observed after heating, where the films were observed to undergo structural transformation at 425 K. This structural change was not observed in the case of $MASnI_3$. The heating treatment increased the conductivity of $CsSnI_3$ by about 4 orders of magnitude and at the same time the materials' color was observed to change from greenish to black with a metallic luster. Additionally, the conductivity of the Cs-based sample was observed to increase with decreasing temperature in a similar trend, which is usually observed for metals [39].

In 2013, Stoumpos et al. [40] calculated the electronic properties of the of different Sn perovskites using the Seebeck coefficient and Hall effect measurements. An exceptionally high electron mobility of $MASnI_3$ was calculated, up to 2320 cm^2 $V^{-1}\cdot s^{-1}$. In 2016, Ma et al., reported that $MASnI_3$ may have opto-electronic properties that are better than those of $CH_3NH_3PbI_3$ [26]. They reported long carrier diffusion lengths of about 300 nm for electrons and 200 nm for holes (and can increase 10 times when the SnF_2 reducing agent was used), which were recorded using time-resolved fluorescence spectroscopy [26]. On the other hand, an interesting slow relaxation of the hot carriers (0.5 ps) was observed for the same samples [26]. Fang et al. [41] also found that the hot carriers in $FASnPbI_3$ have lifetimes of a few seconds, which can be utilized to design solar cells with PCEs that can exceed the Shockley–Queisser limit [27]. Additionally, with increased excitation source power, they observed a 75 meV blue shift of the optical bandgap at room temperature, which is due to the filling of band edge states [41]. However, the electronic properties are very dependent on the preparation method, which may directly affect the material quality and stoichiometry [40,42].

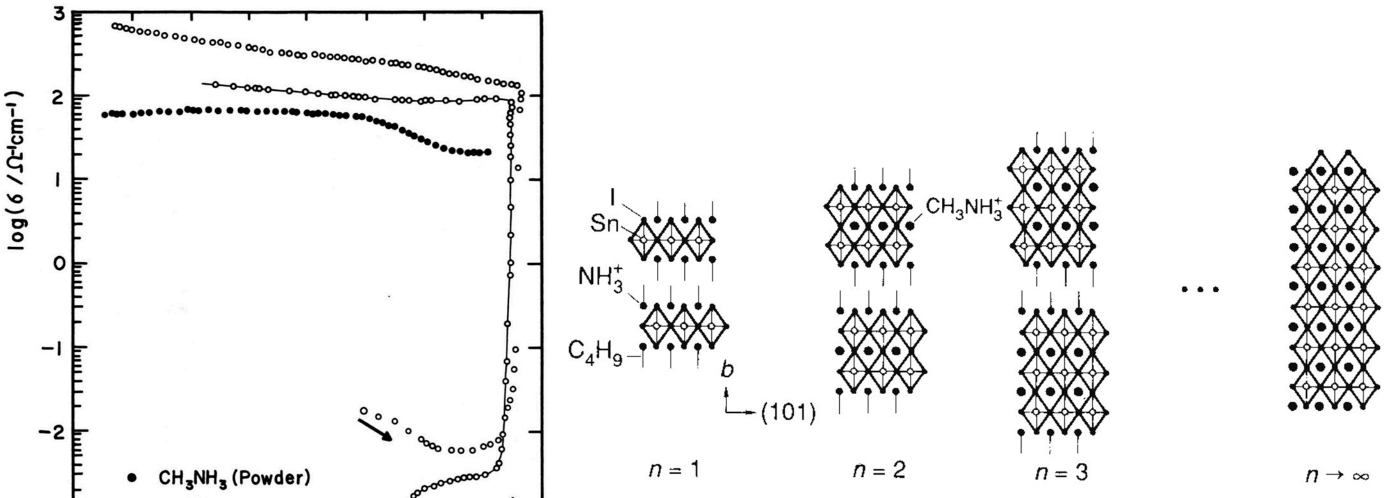

(**a**) (**b**)

Figure 1. (**a**) Electrical conductivity as a function of temperature of $CsSnI_3$ and $MASnI_3$. Reproduced with permission [39]. Copyright 1990, De Gruyter, and (**b**) schematic representation of BA incorporation in perovskite materials with n = 2, 3, and ∞, reproduced with permission [43]. Copyright 1995, Nature publishing group.

2.2. Metallic to Semiconducting by Incorporation of Different Organic Cations

In 1994, looking for new classes of superconductors, the insertion of organic chains of n-butylammonium (BA) into $MASnI_3$ was performed and investigated by Mitzi et al. [43]. The incorporation of BA in the $MASnI_3$ yielded a semiconducting behavior. With a general formula, $BA_2MA_{(n-1)}\ Sn_{(n)}I_{(3n+1)}$. When n = ∞, the film only consists of $MASnI_3$ and was observed to be also more of metallic. With n = 2, the formula becomes $BAMASnI_3$ and the measured resistivity was observed to be 10 Ω cm at room temperature. With more BA incorporated (smaller n values), a more nonmetallic behavior was observed, (i.e., n = 3) along with a trend of resistivity decrease up to a temperature of 75 K followed by a slow upturn in resistivity with higher temperatures.

Similarly, an FA cation was also incorporated in the same way as BA [44]. Based on the formula $[NH_2C(I){=}NH_2]_2(CH_3NH_3)_m\ Sn_m\ I_{3m+2}$, with higher m values a metallic behavior was observed (Figure 1b). When n, m ⇒ ∞, the material is just $MASnI_3$ [43,44]. Mitzi et al. [45] further investigated the observed metallic behavior of $MASnI_3$. They also observed a low carrier density (p-type metallic behavior) with a hall carrier density of $2 \times 10^{19}\ cm^{-3}$. The resistivity was also observed to decrease with decreased temperature, which is in line with the metallic behavior, with a resistivity at room temperature of about 7 mΩ cm [45]. Moreover, Mitzi et al. [45] also reported that the prepared $MASnI_3$ material has free carrier IR (infra-red) reflectivity with a plasma edge, which confirms the metallic nature of the prepared materials.

After that, in 1997, the same previous group reported that the resistivity of $MASnI_3$ at room temperature in the pure $FASnI_3$ is about three orders of magnitude higher than previously reported [46]. The resistivity at room temperature of $FASnI_3$ was found to be ~7 Ω cm compared to 3 Ω cm in the case of $MASnI_3$. The use of FA resulted in lattice expansion, which was speculated to have an effect on the formation of defects, which would readily produce a shift in the energy levels and affect transport properties [46]. Additionally, FA has an extra NH_2 group compared to MA, which provides an extra site to form an additional hydrogen bond that can contribute to better ordering. In general, the FAMA system was also observed to add additional freedom to tailor the electronic properties of such materials by changing the ratio from MA to FA [46].

2.3. Importance of Preparation Method

Several comparative studies of $CsSnI_3$'s electrical behavior and a detailed investigation of MA and FA compared to Cs-based -SnI_3 perovskites were reported [24,42,47]. However, the preparation method and post-treatment can majorly alter the film electronic nature up to even an n-type semiconductor [40]. Two of three methods used to prepare Cs, FA, and MA-SnI_3 perovskites (single crystals from solution, and compressed pellets from sealed tubes dry reaction) exhibited high resistivity trends that are consistent with semiconductor behavior [40]. However, similar samples prepared using the third method (dry in an open tube) were found to behave as a p-type metal. The single crystals from the solution method of FA and MA-SnI_3 were found to be n-type semiconductors with a low level of electron carriers in the temperature range from 300 to 400 K. However, pressed pellets from the dry method with no annealing were found to be p-type semiconductors. When high-quality ingots of $CsSnI_3$ were prepared, superior performance with lifetimes approaching 6.6 ns and diffusion length approaching 1µm compared to only 54 ps and 16 nm for the lower quality polycrystalline ones were observed [25]. For these ingots, no reducing agents such as SnF_2 were used. Based on the extracted lifetimes and diffusion lengths of these high-quality $CsSnI_3$ crystals, a PCE of 23% was estimated [25]. It was shown that the significant factor for electrical properties of the Sn perovskites is the easy oxidization of Sn^{+2} and the formation of the more stable Sn^{+4}. Consequently, p-type metal character and low resistivity are increased, contributing to the self-doping mechanism. Sn has two active electrons on the 5-S orbital, which causes the easy oxidization from Sn^{+2} to Sn^{+4}. It tends to lose these two electrons because the fully occupied 4d orbital electrons are less effective as electromagnetic shields [48].

2.4. Defect Physics of Sn Perovskites

Tin-based perovskites have a direct bandgap, meaning that the momentum of the VB maximum and the CB minimum is the same [10]. This results in a high absorption coefficient. However, it is reported to be an order of magnitude less than Pb-based perovskites [10,26,49]. Even though Sn perovskites have a direct bandgap, their energy bands are higher than those of Pb-based perovskites (Figure 2a). As a result, the Sn-I bond can be broken easily, allowing for I^- and Sn^{+2} to react with H_2O and O_2, respectively; therefore, the Sn perovskites may easily become poor in crystal quality and photovoltaic performance and the properties may be easily altered.

In Sn^{+2} states, the 5P orbital's high energy causes Lewis acidity [50], which leads to the unwanted and uncontrolled rapid crystallization of perovskites. This leads to a substantial amount of physical defects in crystal lattice, which may be the reason for the often observed discrepancy of Sn perovskite properties, such as the energy levels measured and reported values of Sn perovskite films (Figure 2b). LaMer's classic crystal growth theory states that small crystal grains could form due to fast crystallization [51]. These grains significantly affect the optoelectronic properties of Sn-based perovskites since it helps to ease the losses of Sn ions [52]. On the other hand, the oxidization from Sn^{+2} to Sn^{+4} leads to the formation of Sn vacancies (V_{Sn}) and act as high p-doping. Finally, these defects result in hole carriers with high concentrations, which operate as recombination centers for charge carriers. Consequently, tin-based perovskite systems perform sub-optimally.

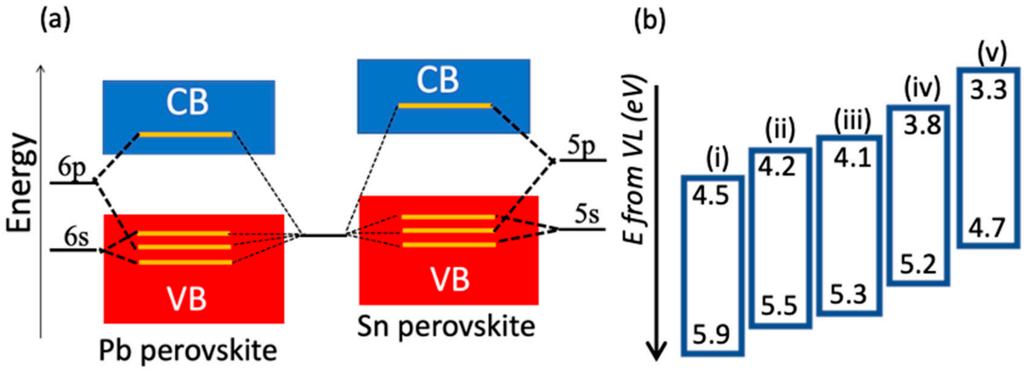

Figure 2. Energy of Sn perovskite bands compared to Pb perovskite and often observed discrepancy of measured and reported values of Sn perovskites' properties, manifested in the bandgap, and the position of valence and conduction bands (VB and CB, respectively) with respect to vacuum level (VL). (**a**) Higher energy band of Sn-perovskites, and (**b**) Discrepancy of energy reported values of $FASnI_3$ (**i**) [53], (**ii**) [54], (**iii**) [55], (**iv**) [56], and (**v**) [57].

3. Stability of Sn Perovskites

The low environmental stability of Sn perovskites has been long recognized as a significant issue, and it has been blamed for their inability to achieve performance comparable to Pb-based PSCs. Perovskite layers tend to oxidize rapidly with oxygen in ambient conditions [58,59]. As a result, short carrier lifetimes and a high nonradiative carrier recombination rate are often observed and detrimental to their photovoltaic performance. There are several factors leading to the well-known poor stability of the Sn-based perovskites, including extrinsic and intrinsic factors. We will discuss specifically the following factors: oxygen, moisture, illumination, and ion migration.

3.1. Moisture Effect

Moisture is considered to be the most prominent factor that causes the degradation of the Sn-based perovskites, leading to the oxidation of Sn [60]. In the presence of moisture, the perovskites are expected to degrade to form metal iodides (i.e., SnI_2). Simultaneously, in the case of MA cations (CH_3NH_3I), they form HI acid under H_2O environments. Even though minimal moisture is necessary to decompose the organic part, an excess is needed to break down the HI and CH_3NH_2 derivatives for the degradation to progress.

In addition to MA cations, FA cations also have a hygroscopic nature [61,62]. FA and MA cations also react with H_2O in distinct binding mechanisms [63]. FA and H_2O form stronger hydrogen bonds (than MA^+), increasing the size of the perovskite lattice and reducing the stability of the crystal structure. However, this may reduce the H_2O interaction with SnI_2. Furthermore, the changes that happen to the electronic properties of $FASnI_3$ and $MASnI_3$ in the presence of moisture air include the fact that the resistivity decreases at the beginning of air exposure for both films and then increases over time [63]. After 40 min of air exposure with 60% humidity, the MA perovskite displays a drop in order of magnitude. On the other hand, the FA perovskite displays a 10% drop under similar conditions (Figure 3a,b).

When TPSCs are tested in nitrogen-filled gloveboxes with H_2O ~ 1 ppm, the performance of $FASnI_3$ devices is more stable and they display good reproducibility (Figure 3c). Therefore, it may be possible to produce better TPSCs by carefully selecting the organic cation, which reduces moisture ingress [64].

3.2. Oxygen Effect

Oxygen damages the charge neutrality of the perovskite structure and causes it to disintegrate into oxides or hydroxides of Sn and MAI or FAI, and as a result the electron–hole recombination increases [10]. The organic cations (i.e., FA and MA) have a significant impact on the O_2-induced degradation of Sn-based perovskites, as well as affecting the optical and electronic properties of the materials such as charge mobility, band alignment, and diffusion length [63]. Lanzetta et al. [65] defined the mechanisms underlying the degradation of different dimensional tin–perovskite films based on phenethylamine $(PEA)_{0.2}(FA)_{0.8}SnI_3$. As a result of moisture and oxygen, SnI_4 and SnO_2 were formed and resulted in the formation of molecular iodine, which is detrimental to the perovskites' performance. Iodine is a hyper aggressive compound that can further oxidize the perovskite, resulting in a cyclic degradation (Figure 4a) [65,66].

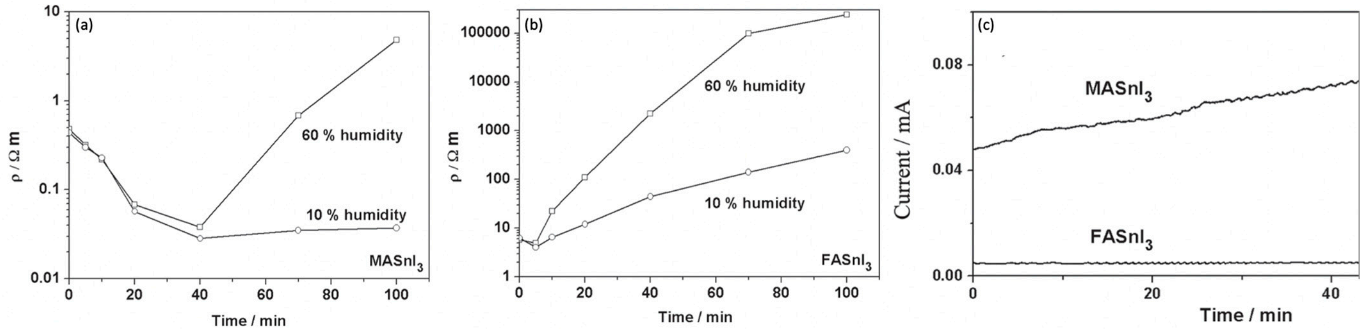

Figure 3. As a function of time and humidity, the resistivity of (**a**) $MASnI_3$ and (**b**) $FASnI_3$. (**c**) In a glovebox in the dark, the $MASnI_3$ and $FASnI_3$ conductor structures were characterized by the current they carry when biased by 1 V. Reproduced with permission [63]. Copyright 2016, WILEY-VCH.

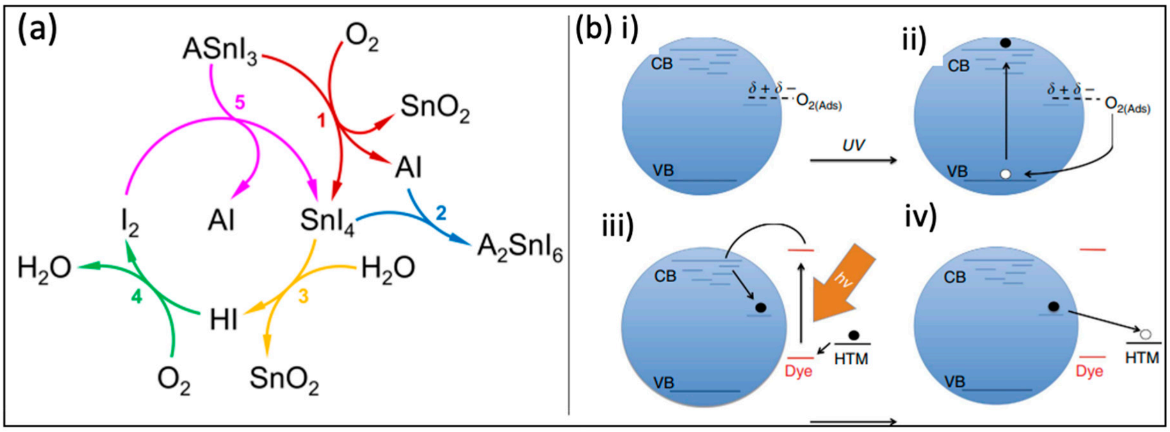

Figure 4. (**a**) Cyclic degradation of tin iodide perovskite in the presence of humid air in which reaction 1 is the oxidation of $ASnI_3$ By O_2, reaction 2 is the solid-state formation of A_2SnI_6, reaction 3 is the hydrolysis of SnI_4 by H_2O, reaction 4 is the oxidation of HI By O_2, and reaction 5 is the oxidation of perovskite by I_2. Reproduced under terms of CC-BY [65]. Copyright 2021, Nature publishing group. (**b**) Proposed ultraviolet light degradation process when photo-generated holes are applied externally with oxygen, after which they react with oxygen radicals adsorbed on the surface of oxygen vacancies, as seen in (**i**,**ii**). As a result of the oxygen, deep surface traps remain unfilled, and each trap has a free electron. (**iii**) As a result of the sensitizer's photoexcitation, electrons flow into the conduction band, where they are deeply trapped, or directly into the deep surface traps, and as a result of that the electrons are strongly trapped and they easily recombine with holes in the spiro-OMeTAD (2,2′,7,7′-Tetrakis[N,N-di(4-methoxyphenyl)amino]-9,9′-spirobifluorene) hole transporter layer (**iv**). Reproduced with permission [67]. Copyright 2013, Nature publishing group.

3.3. Illumination

In general, TiO_2 is one of the most common electron transport materials (ETMs) for n-i-p PSCs. Specifically, under UV-illumination, TiO_2 molecules are a typical photo-catalyst that can accelerate the degradation of perovskite materials [67]. TiO_2 has many several oxygen vacancies as it is an n-type material. In the presence of oxygen, it adsorbs these vacancy cites due to the reaction with the deep electrons that lie in the vacancies. Through UV-illumination, an electron–hole pair was formed in TiO_2. As a result, the electron in the vacancy, which lies before the CB by ~1 eV, will interact with holes in the VB. This operation leads to free electrons in the CB and empty oxygen vacancies with a positive charge, which will act as traps for electrons generated from perovskite material. Additionally, in the common n-i-p structure, spiro-OMeTAD hole transport material (HTM) is used as a heavily p-doped material that will allow for recombination with these free electrons in the CB (Figure 4b(ii–iv)). Lee et al. [68] mitigated this problem in PSCs replacing mesoporous TiO_2 with a thin layer of insulating Al_2O_3. However, with this UV-related problem and with the aforementioned TiO_2-related problems, the p-i-n structure is more commonly used for TPSCs.

One of the popular methods to improve the illumination stability of Sn perovskites is with 'X' site (ABX_3 perovskites) doping, which is unfortunately more susceptible to illumination degradation due to phase separation under illumination [69]. Additionally, the 'A' organic cations, especially MA^+ (best for highest PCEs), are very prone to decomposition under illumination [70,71]. Therefore, 'A' site manipulation or additives are the most popular methods to enhance the Sn perovskites' stability under illumination [72].

3.4. Ion Migration

Ion migration is a well-known and an undesirable phenomenon in PSCs. This is also related to the hysteresis in current density-voltage (J-V) characteristics curve [73]. Due to the dissociation of the charged ions, the diffusion of the ions results in unbalanced charge transport [74]. It also has an impact on the cell's long-term stability and performance, as well as its photoelectronic properties. Defects/ions such as iodide vacancies can migrate across the contact during PSC operation, producing interfacial deterioration, compromising device function, and even triggering device failure. The activation barrier of hybrid perovskites is low. Thus, the ions, such as iodide, are induced to migrate through perovskite devices under applied bias or irradiation [73]. The ions of the iodide (I^-) easily move to defects in perovskites under an external electric field [75]. Additionally, excess iodide may accumulate at the interface between the perovskite, charge transport materials, and electrodes. As a result, the solar cells perform poorly and degrade rapidly [76].

One common method to restrict the ion migration is using additives. For example, the addition of polyvinyl alcohol (PVA) polymer to the $FASnI_3$ solution was shown to improve hydrogen-bonding interactions. Therefore, the PVA-inhibited transport of iodide ions prevented the formation of iodide vacancies, and lowered ionic conductivity, preventing ion migration and preserving the long-term stability of tin-based PSCs [77]. More examples of the recent development of enhanced stability are presented in a later section.

4. Basic Structure and Charge Transport Materials for Tin-Based Perovskite Solar Cells

A typical PSC consists of five main individual layers deposited consecutively on a glass or flexible substrate. Based on the order of the deposited layers on the transparent conductive electrode (TCE), it can be a normal or an inverted structure. The normal structure is TCE/ETM/perovskite absorber (PVSK)/HTM/top electrode (n-i-p stack). The inverted structure is TCE/HTM/PVSK/ETM/top electrode (p-i-n stack).

One of the first TPSCs with the n-i-p structure was reported by Hao et al. [11] with a standard architecture of fluorinated tin oxide (FTO)/compact TiO_2/$MASnI_3$/spiro-OMeTAD/Au and achieved a PCE of 5.7%. The first TPSC with a p-i-n structure was reported with indium tin oxide (ITO)/poly(3,4-ethylenedioxythiophene):polystyrene sulfonate (PEDOT:PSS)/$FASnI_3$/fullerene (C_{60})/2,9-dimethyl-4,7-diphenyl-1,10-phenanthroline (BCP)/Ag with PCE of 6.22% (Figure 5) [53]. These structures had low efficiencies with many problems and challenges, such as poor and uncontrolled quality of Sn perovskites as well as poor interfacial contact resulting in instability problems, mismatch of energy levels, insufficient charge extraction, and hysteresis effect. However, inverted (p-i-n) TPCSs exhibited a slightly better performance, stability, lower cost, as well as ease of fabrication, which made them more reliable to fabricate.

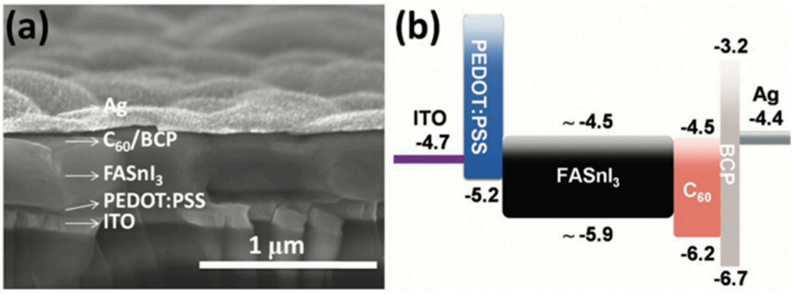

Figure 5. (**a**) SEM image of an inverted FASnI3 perovskite solar cell with SnF2 additive at 10 mol%. (**b**) System energy level diagram of FASnI3. Reproduced with permission [53]. Copyright 2016, WILEY-VCH.

4.1. Electron Transport Layer (ETL)

The ETL is necessary to transport photo-generated electrons from the perovskite layer towards the anode. One of the most common ETLs is the compact blocking layer of TiO_2, which is usually deposited using spray pyrolysis and it has a good chemical stability, electrical properties, and is non-toxic [78]. However, TiO_2 implies high-temperature processing, low durability due to brittle nature, and is a photocatalyst that tends to adsorb oxygen, which results in the degradation of perovskites upon UV intake. Due to this problem, researchers attempt to find alternatives for TiO_2. One of the possible alternatives is ZnO, which exhibits a suitable bandgap, similar to TiO_2 (3.2 eV). It also has a high electron mobility equal to ~200 $cm^2\ V^{-1}\ s^{-1}$ [79]. However, ZnO has a poor stability and is hygroscopic, which makes it less suitable due to its degradation and fast reaction with air [80]. Another rising alternative is SnO_2, which has a high electron mobility (250 $cm^2\ V^{-1}\ s^{-1}$, which is higher than that for TiO_2 and ZnO) [79]. Its bandgap is wider (3.8 eV), which is more suitable for matching with the perovskite materials' bandgap [80,81]. In addition, it is less hygroscopic, which results in lower photocatalytic activity and therefore stable performance [82–84]. An example from 2018, SnO_2 with a thin layer of C_{60} as ETM in n-i-p TPSCs with the architecture of ITO/SnO_2/C_{60}/$FASnI_3$/spiro-OMeTAD/Ag was able to achieve 4.34% without noticeable problems [85].

The most common ETM material used in inverted devices is C_{60} and [6,6]-phenyl-C61-butyric acid methyl ester (PCBM). Fullerenes show a good band alignment with perovskite materials, leading to lower charge recombination since it transfers smoothly to the perovskite [86,87]. It also has a good energy alignment with the CB of the $FASnI_3$ perovskites. Furthermore, using C_{60} as ETM exhibits low hysterias in the *J-V* curve, leading to a high PCE [88].

4.2. Hole Transport Layer (HTL)

The most common hole transport layers (HTLs) that are used in high-performance PSCs are spiro–OMeTAD [89], poly[bis(4-phenyl)(2,4,6-trimethylphenyl)amine] (PTAA) [90,91], PEDOT:PSS [90,92,93], and some metal oxides as well as small molecules [90,94]. HTM plays a significant role in the hole transport and stability of the perovskite layer [95]; however, pure spiro-OMeTAD exhibits low conductivity [96]. Different small molecules are often added as p-dopants, such as lithium salt Lithium bis(trifluoromethanesulfonyl)imide (Li-TFSI) and 4-tert-Butylpyridine (tBP) [97]. Adding these molecules improves the hole mobility, and as a result, high open-circuit voltage (V_{OC}) and PCE were achieved [98,99]. However, due to high moisture sensitivity of Li-TFSI and tBP, the combination results in degradation; additionally, tBP can dissolve perovskites [89]. In order to solve these issues, researchers introduced a set of alternatives such as PEDOT:PSS [100], which is more common in inverted devices. However, PEDOT:PSS is sensitive to moisture, leading to stability problems. One of the alternatives investigated by Cao et al. [101] was copper thiocyanate (CuSCN), with which a PCE of 7.34% was achieved. Nickel oxide (NiO) is also a common HTM and has the advantage of more stability than another alternatives. On the other hand, it has a wide bandgap and good energy alignment with the Sn perovskite [102].

5. Thin Films of Sn Perovskites towards High Efficiency and Stability

Compared to Pb-based PSCs, TPSCs exhibit a much lower PCE, mainly due to the poor film quality, correlated degradation, and detrimental effects. Perovskite films are often fabricated from solutions due to ease of fabrication. In order to create a high-performance tin-based PSC, it is imperative to form dense, compact, well-crystalline perovskite films [103]. Many ways have been proposed to resolve the instabilities of tin-based perovskites. The first step to enhance the stability of the device is to gain a deeper understanding of the degradation mechanisms. Earlier, we briefly pointed out the effects of moisture, oxygen, illumination, ion migration, and chemical reactions which are the most common causes of degradation in perovskite halides. In this section, we go over the most effective ways for increasing the performance and stability of Sn-based perovskite halides that have been reported.

5.1. Tin Perovskites with Additives/Reducing Agents

A defect is often induced by the fast oxidation of Sn^{+2} due to its fast kinetics of nucleation and growth in perovskites; therefore, additives that often reduce the fast oxidation and improve the film morphology (compactness) are required. Sn halides (SnF_2, $SnCl_2$, $SnBr_2$, and SnI_2) and several organic molecules have been shown to prevent oxidation and enhance the performance of TPSCs. Furthermore, Sn halide additives are able to compensate for Sn vacancies in the films, improving the film morphology, reducing the likelihood of vacancy formation, and reducing the background hole density [104].

5.1.1. SnF_2 Additive

One of the first reports of reducing agents was implemented in 2012 by Chung et al. [24] using $CsSnI_3$ Sn perovskites as an HTM by doping with SnF_2 in dye-sensitized solar cells, which helped in producing a V_{OC} of 0.42 V and an overall PCE of 0.9%. Following this, in 2014 Kumar et al. [105] found that incorporating SnF_2 into $CsSnI_3$ reduces the formation energy of Sn vacancies, leading to less conductivity in $CsSnI_3$, and as a result, the TPSCs gained a high current density (J_{SC}) of 22 mA cm^{-2}. The impacts of SnF_2 doping in $FASnI_3$ with 20% mole were confirmed with X-ray diffraction (XRD) data that indicated a reduced amount of Sn^{+4} [42]. This helped the current density to increase by 10 mA cm^{-2}. In 2018, Xiao et al. [106] were able to achieve homogeneous crystal growth and uniform film coverage. They demonstrated that SnF_2 can reduce Sn vacancy (V_{Sn}) concentrations by boosting their formation energy. Following that, Hartmann et al. [107] studied the electronic structure of $CsSnBr_3$ and observed that Sn oxidation was inhibited by the addition of 20% mole SnF_2. In 2016, Ma et al. [26] showed that SnF_2 had the effect of a distinguishable increase in carriers' lifetime from 0.7 ns to 6 ns. Additionally, hole diffusion length was estimated to increase substantially, as a result of the addition of SnF_2, whereas the electron diffusion length remained unchanged. SnF_2 is commonly used in most tin-based photovoltaic systems for easy optimization of Sn perovskites.

5.1.2. $SnCl_2$ Additive

An additional reducing agent commonly used in Sn perovskites is $SnCl_2$ [108]. It was used to increase the stability of the Sn-based devices in an HTM free structure. Using X-ray photoemission spectroscopy (XPS) analysis on $CsSnI_3$ perovskite samples treated with the addition of 10 mol% of $SnCl_2$, they found that $SnCl_2$ was present at the perovskites' surfaces, and that the $SnCl_2$ layer could act as a dryer to improve the stability of $CsSnI_3$. Interestingly, after 5 months of storage under a nitrogen environment, the PCE was observed to increase, along with the V_{OC} and FF. This improvement in the performance over time can be explained by the $SnCl_2$ doping on the electron-transport layer of the used ETM (i.e., PCBM). In addition, they evaluated different tin halide additives ($SnCl_2$, $SnBr_2$, SnI_2, and SnF_2) to see how they could affect HTM-free TPSCs (ITO/$CsSnI_3$/$PC_{61}BM$/BCP/Al). Among the tested devices, with the $SnCl_2$ additive, a PCE of 3.56% was the best, and $SnCl_2$ resulted in the highest film stability. Performance improvements may be attributable to the enhancement of PCBM ETM crystallization under light illumination.

5.1.3. Hydrazine Additive

Hydrazine has long been used in chemical synthesis to prevent oxidation (reducing agent). Additionally, hydrazine's highly volatile nature makes it an easy agent to be introduced as a reducing atmosphere. Song et al. [60] introduced hydrazine vapor atmosphere prior to the spin-coating process of the perovskite precursor. The films were formed in hydrazine atmosphere resulting in reduced defects, oxidation, and therefore better performance. Similarly, Kayesh et al. [109] were able to minimize the concentration of Sn^{+4} by 20% and significantly suppress carrier recombination during the fabrication of $FASnI_3$ perovskite films, by incorporating hydrazinium chloride (N_2H_5Cl) into a single precursor solvent system. A high PCE with significantly enhanced V_{OC} and pinhole-free $FASnI_3$ perovskite films were achieved. Li et al. [110] reported a solution–deposition method for the fabrication of $MASnI_3$ that included hydrazinium iodide (N_2H_5I) with SnI_2 precursor. A mesoporous TPSC with a PCE of 7.13% was achieved.

5.1.4. Acidic Additives

Hypophosphorous acid (HPA). In the synthesis of tin-based perovskites, HPA has long been used as a common reducing agent. In most circumstances, HPA is utilized as an assisting reducing agent in antioxidation when powerful agents such as hydroiodic acid (HI) or SnF_2 are present, eventually stabilizing the process. Researchers used HPA as a coordinating agent in the $CsSnIBr_2$ production process, which allowed them to speed nucleation while restricting Sn^{+2} oxidation. Charge carrier density and Sn vacancy levels were lowered as a result of the HPA integration [111].

2,2,2-trifluoroethylamine hydrochloride (TFEACl). In combination with SnF_2, 5 mol% of TFEACl was found to improve and enhance $FASnI_3$ solar cells [100]. The work function of perovskite films may be adjusted by adding Cl. Therefore, the perovskite films are better aligned with the charge transport layers. In addition, light soaking stability was found to be improved, which all resulted in improved device performance and charge collection.

Gallic acid (GA).Wang et al. [112] used the antioxidant GA as an additive together with excess $SnCl_2$. GA was found capable to form a complex with $SnCl_2$ that is evenly distributed on perovskite grains. The characteristics of the GA can be derived from the aromatic ring's hydroxyl groups (–OH), which can donate electrons and absorb oxygen by hydrogen atoms. The $SnCl_2$ layers present atop perovskite grains were expected to result in a wider bandgap compared to the bulk. After 1000 h of air exposure, unencapsulated GA-based devices preserved more than 80% of their initial PCE, which is one of the highest reports. Moreover, the solar cells with GA exhibited a high PCE of 9.03%.

Ascorbic acid (AA). It is a simple but effective additive that inhibits the oxidation of Sn^{+2} also regulates its film crystallization and creation, and can be utilized to build polymer-stabilized Pb/Sn binary PSCs [113], enhancing the optoelectronic quality of dual, perovskite films greatly. The resulting $MA_{0.5}FA_{0.5}Pb_{0.5}Sn_{0.5}I_3$ film's photogenerated carrier lifetime (183 ns) demonstrates this. As a result, $MA_{0.5}FA_{0.5}Pb_{0.5}Sn_{0.5}I_3$ treated with AA achieved a high PCE of 14.01% and a higher stability than the control device employing the SnF_2 additive, outperforming it. This research proposes a novel method for improving the performance and obtaining more stable Pb/Sn-PSCs.

5.2. Surface Modifiers

There are many surface modifiers for TPSCs that are applied using different methods and can be applied before or after the perovskite layer deposition. Controlling the surface terminations can majorly affect the stability and morphology [59,114,115].

One of the common examples is the introduction of antioxidant-carrying 4-fluorobenzohydrazide (FBH) on top of $FASnI_3$ perovskite films [116]. The C=O group in such modifier was observed to interact with Sn^{+2} and promote the formation of largely oriented perovskites. Additionally, it was found that FBH results in the reduction in Sn^{+4} by the hydrazide group. According to the performed density functional theory calculation, the oxygen absorption barrier is increased after the FBH modification, resulting in a delay in the oxidation process. As a result of such, the interface modifier (capping layer) in the PCE increased from 8.34% to 9.47%.

Similarly, a dense layer of Al_2O_3 as a buffer layer separating perovskites and HTL can prevent degradation from moisture [117]. Cetyltrimethylammoniu bromide (CTAB) doped zirconium oxide (ZrO_x) can also act in a similar manner [118]. In general, the switch from Pb to Sn affects the morphology severely due to the higher Lewis acidity of Sn^{+2} compared to Pb^{+2} [50]. Therefore, one of the major goals when making Sn films is to achieve compact and pinhole-free thin films.

5.3. Cation Engineering

Cations play a major role in Sn halide perovskites thin films in regard to lattice strain engineering. Nishimura et al. [119] investigated the relationship between lattice strain in tin-based perovskite films and TPSCs efficiency. They prepared tin-based $Q_x(FA_{0.75}MA_{0.25})_{1-x}SnI_3$ perovskites, where Q is various cations with different ionic radii such as Na^+, K^+, Cs^+, BA^+, and ethylammonium (EA^+). The link between actual measured lattice strain and solar performance was explored. As the tolerance factor approached unity, the lattice strain decreased (measured by the Williamson hall plot of XRD data). As the lattice strain decreased, the performance of the Sn perovskites was enhanced. $EA_{0.1}(FA_{0.75}MA_{0.25})_{0.9}SnI_3$ with the lowest lattice strain yielded the best performance, because carrier mobility increased as lattice strain decreased. These lattice strains would disrupt carrier mobility and reduce solar cell performance [119]. The lowest lattice strains were found for Cs-0.1 and EA-0.1 and provided the highest mobility of about 43 $cm^2\ V^{-1}{\cdot}s^{-1}$; however, in the case of Na-0.1, the lattice strain was found to be higher and therefore the mobility was down to 4.6 $cm^2\ V^{-1}{\cdot}s^{-1}$.

Sun et al. [120] added a bi-linkable reductive cation (i.e., formamide (FM)), into $FASnI_3$ to function as molecular glue for improving the stability and performance of TPSCs by the formyl group (–CHO) and amine group ($-NH_2$). They revealed that the NH_2 and C=O groups in FM are capable of interacting with FA^+ and Sn^{+2} through hydrogen bonds and Lewis acid–base coordination, respectively. This resulted in a greater grain size, preferred orientation, lower defect density, and better film stability. The TPSC device based on 10% of FMI resulted in a 40% increased PCE from 5.51% to 7.71% with notable enhanced stability, retaining its initial PCE after one year in N_2 without encapsulation.

Jokar et al. [17] used guanidinium cations (GA^+) as an additive with at least 1% of ethylenediammonium diiodide ($EDAI_2$) to form a $FASnI_3$ films, and this resulted in the remarkably improved performance of TPSCs. A high PCE of 8.5% was achieved and increased to 9.6% after 2000 h of storage in a glove box. Additionally, the resulting perovskite operated for almost an hour under continuous illumination and for six days in air without encapsulation [17].

5.4. Solvent Engineering

Solvents and secondary solvents can play a major role in the formation of pinholes in thin films, especially thin films that contain organic materials [121]. One common way to produce a compact Sn film is by different solvents, such as dimethylformamide (DMF) or dimethyl sulfoxide (DMSO) [122,123]. Post-treatment with antisolvents also plays a crucial role in the quality of tin-based perovskite films [123,124].

It was reported that when perovskite films are formed without any anti-solvent dripping, the precursor is far from supersaturated until the solvent totally evaporates and, as a result, the nucleation site density is rather low, resulting in a flower-like film with limited surface coverage [123]. Therefore, different antisolvents (diethyl ether (DE), toluene (TL), and chlorobenzene (ClB)) were tested. The size of pinholes in the $FA_{0.75}MA_{0.25}SnI_3$ films dripped by DE is less than that of pinholes in the film dripped by TL, but the quantity of pinholes is greater. In the case of ClB, the film has a uniform surface with full coverage and clear grain features. One reason for this could be related to its high boiling point of 131 °C, which has a slower evaporation rate, which extends the crystal development period during the thermal annealing process.

Hao et al. [42] investigated the DMSO function as a the Lewis base solvent to adjust the crystallization rate of $MASnI_3$ perovskite by Lewis acid–base interaction. When DMSO molecules react with Lewis acid SnI_2, they form the SnI_2-3DMSO intermediate adduct, which effectively slows down the interaction between MAI and SnI_2, resulting in an enhanced $MASnI_3$ film. Similarly, the generation and orientation of $FASnI_3$ perovskites was controlled when poly-ethylene-co-vinyl acetate (PEVA) was introduced into the anti-solvent [125]. At the grain boundaries, the C=O groups of PEVA molecules cause a complexation between Lewis acid–base interaction and Sn^{+2}. This results in larger grains and lowered surface defects of $FASnI_3$, leading to enhanced devices' performance.

5.5. Low-Dimensional Perovskites

In fact, using different solvents incorporated with different additives as well as cations with different radii often has a direct influence on the dimensionality of the perovskite films, which is on its own is a major research and development direction. Lower dimension perovskites seem to be more stable than three-dimensional ones, so these are expected to improve tin-based perovskites' stability [126]. The three-dimensional structure of perovskites could be decreased to two- or one-dimensional by substituting the bulky organic ammonium ions at the A-site in the perovskite lattice or by inserting 2D materials in the precursor solution [127,128]. 2D perovskites seems to have exceptional optoelectronic properties and therefore may make them excellent photovoltaic materials [129]. 2D perovskite reduces moisture as well as oxygen from going inside the film [130,131]. It also can reduce defects, resulting in a low amount unwanted self-doping [132]. Many researchers are currently investigating 2D TPSCs to increase their stability based on the benefits of lower dimension perovskites.

Similarly, low-dimensional Sn perovskites have become a topic of interest in TPSCs due to their ability to improve device performance and stability. In 2017, Liao et al. [133] incorporated phenylethylammonium (PEA) into $FASnI_3$ perovskites and they achieved perpendicularly oriented, low-dimensional Sn perovskite films with remarkably enhanced stability and a PCE of 5.9%. In 2020, a report by Liang et al. [134] utilizing indene-C_{60} bisadduct (ICBA) as an ETM found that their Sn-based perovskite ($PEA_x\,FA_{1-x}SnI_3$) with PEA incorporation formed a low-dimensional perovskite with reduced defect concentrations, which resulted in a high V_{OC} of 0.94, a record PCE of 12.4%, and better stability (shelf stability of 3800 h).

5.6. Variety of Very Recent Perovskite Additives, Surface/interface Modifiers in TPSCs with Noticeable Performance

There are many additives that were reported in recent years to enhance the performance of TPSCs [55,72,135–137]. However, here (Table 1) we summarize most of the very recent and noticeable additives and correlated outstanding device performance of lead-free TPSCs that were reported during the last two years. Table 2 provides a list of the most recent and highly performing surface/interface modifiers that were applied in lead-free TPSCs. Table 3 provides a list of most recent highly performing mixed Pb-Sn perovskites with Pb $\leq$ 50% and it includes devices with both perovskite additives and surface/interface modifiers. The table also provides structure and reported stability.

Table 1. Best performing Pb-free TPSCs with perovskite additives reported in 2021 and 2022.

Structure	Additive	PCE (%)	Eg (eV)	Stability (Period, Conditions, Percentage from Original Efficiency)	
ITO/PEDOT [a]/$FA_{0.92}PEA_{0.08}SnI_3$/PCBM/Al	MACl	7.1	1.42	42 days, encapsulated, 100+% 6 h, air, 60%	[138]
FTO/c-TiO_2/mp-TiO_2/$CsSnI_3$/P3HT/Au *	MBAA [b]	7.5	1.3	60 days, nitrogen, 60% 5 days, air, 76.5% 5 days, 1 sun, 58.4%	[139]
ITO/PEDOT/$FASnI_3$/C60/BCP/Ag **	FM^+ [t]	7.7%	1.4	367 days, nitrogen, 100%	[120]
FTO/SnO_2/Al_2O_3-Gr [c]/$FA_{0.8}MA_{0.2}SnI_3$/spiro [d]/Au *	rGO [e]	7.7	1.27	30 days air, 42% 30 days, 85%, dry argon	[140]
ITO/PEDOT/$FA_{0.75}MA_{0.10}SnI_2Br$/PCBM/BCP/Ag	PEA^+ [f]	8.0	1.66	63 days, nitrogen, 100% 13 days, air, 100%	[141]
ITO/PEDOT//PCBM/PCB/Ag	F-PDI [s]	9.5	1.42	125 days, 1 sun, nitrogen, 80%	[142]
ITO/PEDOT/$MASnI_3$/PCBM/BCP/Ag	EABr [g]	9.6	1.3	30 days, nitrogen, 93%	[143]
FTO/PEDOT/$FASnI_3$/C_{60}/BCP/Ag	FAAc [h]	10.0	NA	67 days, 1 sun, nitrogen, 82%	[144]
PET/ITO/NiO_x/$FASnI_3$/4AMPI2 [i]/PCBM/BCP/Ag ***	Ge/GeO_2	10.4	1.38	29 days, 1 sun, nitrogen, MPP, 80% 2500 bending cycles, R = 5 mm, 80%	[145]
ITO/PEDOT/$FASnI_3$/C_{60}/BCP/Ag **	DipI [j] and NaBH4 [k]	10.6	1.38	54 days, nitrogen, MPP, 96%	[146]
ITO/PEDOT/$FASnI_3$/PCBM/BCP/Ag	EABr [g]	10.8	1.48	84 days, nitrogen, 82%	[147]
ITO/PEDOT/$FASnI_3$/PAI [l]/C_{60}/BCP/Ag	PEA^+ [f]	12.1	1.4	21 days, 1 sun, MPP, encapsulated, 94%	[148]
ITO/PEDOT/$MASnI_3$/ICBA/BCP/Ag	$CsPbI_3$ QDs [m]	12.5	1.3	40 days, nitrogen, 96% 23 days, 1 sun, 62%	[149]
ITO/PEDOT/$FASnI_3$/ICBA/BCP/Ag	$CsPbI_3$ QDs	13.0	1.4	40 days, nitrogen, 83% 23 days 1 sun, 64%	[149]
ITO/PEDOT/$FASnI_3$+PHCl-Br/C_{60}/BCP/Ag	$PhNHNH_3^+$ and Ph-Cl^- Br^- [n]	13.4	1.4	14 days, 1 sun, 82% 200 days, nitrogen, 91%.	[69]
ITO/PEDOT/$FASnI_3$/ICBA/BCP/Ag	4A3HA [o]	13.4	1.4	83 days, nitrogen, 98% 42 days, at 82 °C, 80%	[150]
ITO/PEDOT/PEAFASn$(IBr)_3$/ICBA/BCP/Ag	GAA [p]	13.7	NA	50 days, nitrogen, 93%	[151]
ITO/PEDOT/$FASnI_3$/BCP-ICBA/Ag	3T [q]	14.0	1.4	30 days, nitrogen, 100% 9 h, air, 85%	[152]
ITO/PEDOT/$FASnI_3$/ICBA/BCP/Ag ****	PEA [f] Br	14.6	NA	100 days, nitrogen, 96%	[153]
ITO/PEDOT/$FASnI_3$/ICBA/BCP/Al	FPEABr [r]	14.8	1.43	19 days, nitrogen, 80%	[154]

[a] PEDOT:PSS (PEDOT), [b] N,N′-methylenebis(acrylamide), [c] Graphene (Gr), [d] spiro-OMeTAD, [e] reduced graphene oxide (rGO), [f] phenylethylammonium (PEA^+), [g] ethylammonium bromide (EABr), [h] formamidine acetate (FAAc), [i] 4-(aminomethyl) piperidinium diiodide (4AMPI2), [j] Dipropylammonium iodide (DipI), [k] sodium borohydride (NaBH4), [l] n-propylammonium iodide (PAI), [m] quantum dots(QDs), [n] phenylhydrazine ($PhNHNH^{3+}$) and phenylhalides (Cl^- and Br^-) (Ph-$Cl^-$$Br^-$), [o] 4-amino-3-hydroxybenzoic acid (4A3HA), [p] 2-Guanidinoacetic acid (GAA), [q] trimethylthiourea (3T), [r] 4-fluoro-phenethylammonium bromide (FPEABr), [s] fluorinated-perylene diimide (F-PDI), [t] formamide (FM), * n-i-p structure, ** one of the best stability records, *** flexible record and with NiO_x HTL, **** with SnI_2-DMSO colloidal complex.

Table 2. Surface and Pb-free. Best-performing Pb-free TPSCs with perovskite surface/interface modifiers reported in 2021 and 2022.

Structure	Treatment	PCE (%)	Eg (eV)	Stability (Period, Conditions, Percentage from Original Efficiency)	
ITO/PEDOT [a]/$CsSnI_3$/C_{60}/BCP/Cu	TSC [b] on SnI_2	8.2	N.A.	21 days, 1 sun, encapsulated, 71%	[155]
ITO/PTAA/$FASnI_3$/C_{60}/BCP/Ag	PEAI [c] on PTAA	8.3	1.4	83 days, nitrogen, 87%	[56]
FTO/PEDOT/$EDA_{0.01}(GA_{0.06}(FA_{0.8}Cs_{0.2})_{0.94})_{0.98}SnI_2Br$/$C_{60}$/BCP/Ag	2PACz[d] on PEDOT	8.7	1.62	70 days, nitrogen, 75%	[156]
FTO/bl-TiO_2/mp-TiO_2/$Cs_{0.1}FA_{0.9}SnI_3$/PTAA/Au *	ThMAI [e] on PVSK	9.1	1.45	35 days, nitrogen, 92%, 6 days, air, 62%	[157]
ITO/NiO_x/$FASnI_3$/PCBM/BCP/Ag	FAAc [f] on PVSK	9.1	N.A.	55 days, nitrogen, 80%	[158]
ITO/PEDOT/$FA_{0.75}MA_{0.25}SnI_{2.75}Br_{0.25}$/PCBM/BCP/Ag	CF_3PEAI [g] on pvsk	10.4	1.45	52 days, nitrogen, 80%, 4 days, air, 80%	[159]
ITO/PEDOT/$FA_{0.98}EDA_{0.01}SnI_3$/C_{60}/Ag	SA [h] + PEDOT on PEDOT	10.5	1.33	83 days, nitrogen, 95%	[160]
FTO/PEDOT/$FA_{0.75}MA_{0.25}SnBrI_2$/ICBA/Bphene [i]/Ag **	KSCN [j] on PEDOT	11.2	1.63	42 days, nitrogen, 80%	[161]
FTO/PEDOT/$FASnI_3$/C_{60}/BCP/Ag	vapor of EDA [k] on PVSK.	11.3	1.42	40 days, nitrogen, 85%	[162]
ITO/PEDOT/$FASnI_3$/C_{60}/BCP/Ag ***	PAI [l] on PVSK	12.1	1.4	21 days, 1 sun, MPP, encapsulated, 94%	[148]
ITO/PEDOT/$FASnI_3$/C_{60}/BCP/Ag	PMMA [m] on PVSK	13.8	1.41	42 days, 1 sun, encapsulated, MPP, 94%	[163]
ITO/PEDOT/$FAMASnI_3$/C_{60}/BCP/Ag	FACl on PVSK	14.7	1.42	42 days, nitrogen, 92%	[164]

[a] PEDOT:PSS (PEDOT), [b] thiosemicarbazide (TSC), [c] phenylethylammonium iodide (PEAI), [d] carbazole with phosphonic acid (2PACz), [e] 2-thiophenemethylammonium iodide (ThMAI), [f] formamidine acetate (FAAc), [g] 3-(trifluoromethyl) phenethylamine hydroiodide (CF_3PEAI), [h] zwitterion, sulfamic acid (SA), [i] bathophenanthroline (Bphene), [j] potassium thiocyanate (KSCN), [k] ethane-1,2-diamine (EDA), [l] n-propylammonium iodide (PAI), [m] poly-methyl methacrylate (PMMA). * n-i-p structure, ** Indoor PCE-record of 17.6% under 1062 lx, *** cold precursor solution (0 °C).

Table 3. Additives/surface and Pb ≤ 50%. Best-performing TPSCs with lead content ≤ 50% with perovskite surface/interface modifiers or perovskites additive reported in 2021 and 2022.

Structure	Additive/Treatment	PCE (%)	Eg (eV)	Stability (Period, Conditions, Percentage from Original Efficiency)	
ITO/PEDOT [a]/$FASn_{0.5}Pb_{0.5}I_3$/C_{60}/BCP/Ag	K-SCN [b] additive	14.5	1.25	5 days, air, 55%	[165]
ITO/PEDOT/$FA_{0.8}MA_{0.15}Cs_{0.05}Pb_{0.5}Sn_{0.5}I_3$/$C_{60}$/BCP/Ag	PEAI [c] additive	17.3	1.25	33 h, air, 85% 45 days, nitrogen, 87%	[166]
ITO/$FA_{0.85}Cs_{0.15}Sn_{0.5}Pb_{0.5}I_3$/PCBM/PCB/Cu *	FSA [d] additive and PEAI [c] in toluene on PVSK	17.4	1.27	20 days, air, 81%	[167]
ITO/PEDOT/$FA_{0.\ 5}MA_{0.5}Pb_{0.5}Sn_{0.5}I_3$/PCBM/$C_{60}$/BCP/Ag	IMBF4 [e] additive	19.1	1.25	42 days, nitrogen, 90% 2 days, 1 sun, 80%	[168]
ITO/PEDOT/$FA_{0.83}Cs_{0.17}Pb_{0.5}Sn_{0.5}I_3$/$C_{60}$/BCP/Ag	PEAI [c] on PVSK	19.1	NA	4 days, nitrogen, 1 sun, MPP 82%	[169]
ITO/NiO_x/$FA_{0.5}MA_{0.5}Sn_{0.5}Pb_{0.5}I_3$/$PC_{61}BM$/BCP/Ag	PFN [f] on NiO_x	19.8	1.26	20 days, air, 68%	[170]
ITO/PEDOT/$FA_{0.7}MA_{0.3}Pb_{0.5}Sn_{0.5}I_3$/PCBM/BCP/Cu.	CA [g] additive	19.9	1.26	21 days, nitrogen, 90%	[171]
ITO/$Cs_{0.05}MA_{0.45}FA_{0.5}Pb_{0.5}Sn_{0.5}I_3$/PCBM/$C_{60}$/BCP/Ag *	Cu-SCN [b] and GlyHCl [h] on ITO	20.1	1.21	42 days, nitrogen, 90% 4 days, 1 sun, MPP, 72%	[172]
ITO/PEDOT/$FA_{0.7}MA_{0.3}Pb_{0.5}Sn_{0.5}I_3$/PCBM/BCP/Ag	[PNA]BF4 [i] on PEDOT	20.1	NA	10 days, nitrogen, 85 °C, 80% 50 days, nitrogen, 90.8%	[173]
ITO/PEDOT/$FA_{0.7}MA_{0.3}Pb_{0.5}Sn_{0.5}I_3$/$C_{60}$/BCP/Ag	PhDMADI [j] additive	20.5	1.25	29 days, nitrogen, 95%	[174]
ITO/PEDOT/$MA_{0.3}FA_{0.7}Pb_{0.5}Sn_{0.5}I_3$/PCBM/BCP/Ag	GUA [k] additive and HAI [l] on PVSK	20.5	1.27	6 days nitrogen, 1 sun, 60%	[175]
FTO/PEDOT/$Cs_{0.025}FA_{0.475}MA_{0.5}Sn_{0.5}Pb_{0.5}I_{2.925}Br_{0.075}$/PCBM/$C_{60}$/BCP/Ag	RbI additive	21.0	1.28	6 days, nitrogen, at 85 °C, 75% 30 days, nitrogen, 99%	[176]
ITO/PEDOT/$FA_{0.5}MA_{0.5}Pb_{0.5}Sn_{0.5}I_3$/$C_{60}$/BCP/Ag	HZBA [m] additive	21.1	1.26	8 days, nitrogen, 90%	[177]
ITO/PEDOT/$Cs_{0.2}FA_{0.8}Pb_{0.5}Sn_{0.5}I_3$/$C_{60}$/BCP/Cu	BaI_2 additive	21.2	1.21	15 days, encapsulated, 1 sun, MPP, 95%	[178]
FTO/PEDOT/$FA_{0.6}MA_{0.4}Sn_{0.6}Pb_{0.4}I_3$/$C_{60}$/BCP/Ag	N,Cl-GQDs [o] at PEDOT	21.5	1.25	42 days, nitrogen, 90%	[179]
ITO/PEDOT/$Cs_{0.05}FA_{0.7}MA_{0.25}Sn_{0.5}Pb_{0.5}I_3$/$C_{60}$/BCP/Ag	BBMS [n] + SnF_2	22.0	1.22	111 days, nitrogen, 60 °C, 98 %	[180]
ITO/PEDOT/$FA_{0.6}MA_{0.4}Sn_{0.6}Pb_{0.4}I_3$/$C_{60}$/BCP/Ag.	PEAI [c] and guanidinium-SCN [b]	22.1	1.25	76 days, nitrogen, MPP, 82%	[181]
ITO/CzAn [p]/PMMA/$FA_{0.8}Cs_{0.2}Sn_{0.5}Pb_{0.5}I_3$/PCBM/$C_{60}$/BCP/Cu	CzAn [p] HTM and BHC [q] on PVSK	22.6	1.22	7 days, encapsulated, MPP, 1 sun, 90% 42 days, encapsulated, 96%	[182]
FTO/$Cs_{0.025}FA_{0.475}MA_{0.5}Sn_{0.5}Pb_{0.5}I_{2.925}Br_{0.075}$/EDA [r]/PCBM/$C_{60}$/BCP/Ag *	2PACz [s] and MPA [t] at FTO	23.3	1.25	42 days, nitrogen, 1 sun, 100%	[183]
FTO/PEDOT/$Cs_{0.1}FA_{0.6}MA_{0.3}Sn_{0.5}Pb_{0.5}I_3$/$C_{60}$/BCP/Ag	$EDAI_2$ [u] on PVSK and GlyHCl [v] at PEDOT	23.6	1.24	8 days, nitrogen, 1 sun, MPP, 80%	[184]

[a] PEDOT:PSS (PEDOT), [b] thiocyanate (SCN), [c] 2-phenylethylazanium iodide (PEAI), [d] formamidine sulfinic acid (FSA) additive, [e] ionic imidazolium tetrafluoroborate (IMBF4), [f] poly[(9,9-bis(30-(N,N-dimethylamino)propyl)-2,7-fluorene)-alt-2,7-(9,9-dioctyfluorene)] (PFN), [g] caffeic acid (CA), [h] glycine hydrochloride (GlyHCl), [i] iso-pentylammonium tetrafluoroborate salt ([PNA]BF4), [j] p-phenyl dimethylammonium iodide (PhDMADI), [k] β-guanidinopropionic acid (GUA), [l] hydrazinium iodide (HAI), [m] 4-hydrazinobenzoic acid (HZBA), [n] 1-bromo-4-(methylsulfinyl) benzene (BBMS), [o] graphene quantum dots (GQDs), [p] poly[(phenyl)imino[9-(2-ethylhexyl)carbazole]-2,7-diyl] (CzAn), [q] benzylhydrazine hydrochloride (BHC), [r] Ethylenediamine, [s] 2-(9H-carbazol-9-yl) ethyl] phosphonic acid (2PACz), [t] methyl phosphonic acid (MPA), [u] ethylenediammonium diiodide ($EDAI_2$), [v] glycine hydrochloride (GlyHCl), * HTL-free.

It is noteworthy to mention that the reasons behind the enhancement of the performance of the devices listed in the tables are often related to the same reasons. Here, we briefly list the reasons behind the enhancement in general, which is important for further future consideration and development to achieve even higher performance: (i) oxidation, (ii) reduced defects, (iii) controlled crystallization, (iv) morphology (compactness and pinholes, strain relaxation), (v) charge diffusion and extraction (mobility, carriers density, energy levels, recombination), (vi) built-in electric field (gradient vertical perovskite growth), (vii) better choice of cations (reduced or eliminated MA^+) (iix) hydrophobicity, and (ix) passivation of the acidic and hygroscopic surface of the commonly used PEDOT:PSS HTL (or alternative or HTL or SAMs).

6. Conclusions and Prospects

Currently, there is a significant amount of research that is being carried out on the enhancement of TPSCs. The PCE of lead-free as well as lead-mixed TPSCs is approaching 15% and 24%, respectively. Similarly, the stability of TPSCs is rapidly improving. It may be true that the PCEs and the stability of TPSCs are still behind lead PSCs; however, TPSCs have a wider range of applications, especially due to the lesser toxicity and narrower bandgap of Sn perovskites.

The development of new and improved synthetic methods for Sn-based perovskite materials can help to further boost the efficiency, stability, and scalability of TPSCs. Further investigation of new device structures can lead to further improvements in efficiency and stability. Investigating the use of new interfaces and interlayers can help to improve the stability and efficiency of Sn-based perovskite solar cells. Improving the stability of Sn-based perovskite solar cells is still a crucial direction for future research. Strategies such as passivation of defects, encapsulation, and material engineering can help to improve their long-term stability.

It is important to emphasize that Sn-based perovskites exhibit both metallic and semiconducting behavior depending on the preparation method. This is attributed to the presence of metallic Sn phases in the perovskite film at different levels. Therefore, different properties can be observed across the film (bottom surface, bulk, and top surface). This behavior can result in a built-in electric field. In general, this varying conducting nature may result in a trade-off between electrical conductivity and photoelectric performance. As discussed, various strategies have been proposed to reduce the metallic Sn content, and recently, there have been several good attempts to control such problem and to use it to make a controlled built-in field and surfaces. In general, there are several challenges facing TPSCs and manifested in the poor stability of Sn. Additionally, the control of crystallization dynamics (growth and gradient), self-doping, morphology, strains, defects density, oxidation, ion migration, and charge transport and extraction all hinder the performance of TPSCs. However, many successful efforts have been made to resolve these issues, such as the use of various additives, surface/interface modifiers, solvents engineering, crystal dimensionality, and compositional engineering, which are all moving forward in the enhancement of the overall PV performance and stability of TPSCs.

This review summarizes some milestones in the development and the up-to-date progress of tin perovskites and TPSCs. The crystal structure and electrical properties of tin perovskite materials, as well as the cause of their chemical instability, were discussed. Furthermore, the main factors affecting the stability and resulting degradation, such as moisture, oxygen, ion migration, and UV-illumination, were summarized.

Funding: This research received no external funding.

Acknowledgments: We would like to thank Birzeit University for their support.

Conflicts of Interest: The authors declare no conflict of interest.

References

1. Jeong, M.; Choi, I.W.; Go, E.M.; Cho, Y.; Kim, M.; Lee, B.; Jeong, S.; Jo, Y.; Choi, H.W.; Lee, J.; et al. Stable perovskite solar cells with efficiency exceeding 24.8% and 0.3-V voltage loss. *Science* **2020**, *369*, 1615–1620. [CrossRef] [PubMed]
2. Green, M.A.; Dunlop, E.D.; Hohl-Ebinger, J.; Yoshita, M.; Kopidakis, N.; Bothe, K.; Hinken, D.; Rauer, M.; Hao, X. Solar cell efficiency tables (Version 60). *Prog. Photovolt. Res. Appl.* **2022**, *30*, 687–701. [CrossRef]
3. Verduci, R.; Romano, V.; Brunetti, G.; Yaghoobi Nia, N.; Di Carlo, A.; D'Angelo, G.; Ciminelli, C. Solar Energy in Space Applications: Review and Technology Perspectives. *Adv. Energy Mater.* **2022**, *12*, 2200125. [CrossRef]
4. Weber, D. $CH_3NH_3PbX_3$, ein Pb (II)-system mit Kubischer Perowskitstruktur/$CH_3NH_3PbX_3$, a Pb (II)-system with Cubic Perovskite Structure. *Z. Nat. B* **1978**, *33*, 1443–1445. [CrossRef]
5. Kojima, A.; Teshima, K.; Shirai, Y.; Miyasaka, T. Organometal halide perovskites as visible-light sensitizers for photovoltaic cells. *J. Am. Chem. Soc.* **2009**, *131*, 6050–6051. [CrossRef] [PubMed]
6. De Wolf, S.; Holovsky, J.; Moon, S.-J.; Löper, P.; Niesen, B.; Ledinsky, M.; Haug, F.-J.; Yum, J.-H.; Ballif, C. Organometallic Halide Perovskites: Sharp Optical Absorption Edge and Its Relation to Photovoltaic Performance. *J. Phys. Chem. Lett.* **2014**, *5*, 1035–1039. [CrossRef]
7. Shi, D.; Adinolfi, V.; Comin, R.; Yuan, M.; Alarousu, E.; Buin, A.; Chen, Y.; Hoogland, S.; Rothenberger, A.; Katsiev, K.; et al. Solar cells. Low trap-state density and long carrier diffusion in organolead trihalide perovskite single crystals. *Science* **2015**, *347*, 519–522. [CrossRef]
8. Assi, M.A.; Hezmee, M.N.M.; Sabri, M.Y.M.; Rajion, M.A. The detrimental effects of lead on human and animal health. *Vet. World* **2016**, *9*, 660. [CrossRef]
9. Needleman, H. Lead poisoning. *Annu. Rev. Med.* **2004**, *55*, 209–222. [CrossRef]
10. Noel, N.K.; Stranks, S.D.; Abate, A.; Wehrenfennig, C.; Guarnera, S.; Haghighirad, A.-A.; Sadhanala, A.; Eperon, G.E.; Pathak, S.K.; Johnston, M.B.; et al. Lead-free organic–inorganic tin halide perovskites for photovoltaic applications. *Energy Environ. Sci.* **2014**, *7*, 3061–3068. [CrossRef]
11. Hao, F.; Stoumpos, C.C.; Cao, D.H.; Chang, R.P.H.; Kanatzidis, M.G. Lead-free solid-state organic–inorganic halide perovskite solar cells. *Nat. Photonics* **2014**, *8*, 489–494. [CrossRef]
12. Stoumpos, C.C.; Frazer, L.; Clark, D.J.; Kim, Y.S.; Rhim, S.H.; Freeman, A.J.; Ketterson, J.B.; Jang, J.I.; Kanatzidis, M.G. Hybrid germanium iodide perovskite semiconductors: Active lone pairs, structural distortions, direct and indirect energy gaps, and strong nonlinear optical properties. *J. Am. Chem. Soc.* **2015**, *137*, 6804–6819. [CrossRef]
13. Krishnamoorthy, T.; Ding, H.; Yan, C.; Leong, W.L.; Baikie, T.; Zhang, Z.; Sherburne, M.; Li, S.; Asta, M.; Mathews, N. Lead-free germanium iodide perovskite materials for photovoltaic applications. *J. Mater. Chem. A* **2015**, *3*, 23829–23832. [CrossRef]
14. Park, B.W.; Philippe, B.; Zhang, X.; Rensmo, H.; Boschloo, G.; Johansson, E.M. Bismuth based hybrid perovskites A3Bi2I9 (A: Methylammonium or cesium) for solar cell application. *Adv. Mater.* **2015**, *27*, 6806–6813. [CrossRef] [PubMed]
15. Hebig, J.-C.; Kuhn, I.; Flohre, J.; Kirchartz, T. Optoelectronic properties of (CH3NH3) 3Sb2I9 thin films for photovoltaic applications. *ACS Energy Lett.* **2016**, *1*, 309–314. [CrossRef]
16. Lee, S.J.; Shin, S.S.; Im, J.; Ahn, T.K.; Noh, J.H.; Jeon, N.J.; Seok, S.I.; Seo, J. Reducing carrier density in formamidinium tin perovskites and its beneficial effects on stability and efficiency of perovskite solar cells. *ACS Energy Lett.* **2017**, *3*, 46–53. [CrossRef]
17. Jokar, E.; Chien, C.H.; Tsai, C.M.; Fathi, A.; Diau, E.W.G. Robust tin-based perovskite solar cells with hybrid organic cations to attain efficiency approaching 10%. *Adv. Mater.* **2019**, *31*, 1804835. [CrossRef]
18. Gil-Escrig, L.; Dreessen, C.; Palazon, F.; Hawash, Z.; Moons, E.; Albrecht, S.; Sessolo, M.; Bolink, H.J. Efficient Wide-Bandgap Mixed-Cation and Mixed-Halide Perovskite Solar Cells by Vacuum Deposition. *ACS Energy Lett.* **2021**, *6*, 827. [CrossRef]
19. Nasti, G.; Abate, A. Tin Halide Perovskite (ASnX3) Solar Cells: A Comprehensive Guide toward the Highest Power Conversion Efficiency. *Adv. Energy Mater.* **2020**, *10*, 1902467. [CrossRef]
20. Chen, M.; Ju, M.G.; Garces, H.F.; Carl, A.D.; Ono, L.K.; Hawash, Z.; Zhang, Y.; Shen, T.; Qi, Y.; Grimm, R.L.; et al. Highly stable and efficient all-inorganic lead-free perovskite solar cells with native-oxide passivation. *Nat. Commun.* **2019**, *10*, 16. [CrossRef]
21. Wang, C.; Gu, F.; Zhao, Z.; Rao, H.; Qiu, Y.; Cai, Z.; Zhan, G.; Li, X.; Sun, B.; Yu, X. Self-repairing tin-based perovskite solar cells with a breakthrough efficiency over 11%. *Adv. Mater.* **2020**, *32*, 1907623. [CrossRef] [PubMed]
22. Nakamura, T.; Yakumaru, S.; Truong, M.A.; Kim, K.; Liu, J.; Hu, S.; Otsuka, K.; Hashimoto, R.; Murdey, R.; Sasamori, T. Sn (IV)-free tin perovskite films realized by in situ Sn (0) nanoparticle treatment of the precursor solution. *Nat. Commun.* **2020**, *11*, 3008. [CrossRef] [PubMed]
23. Gai, C.; Wang, J.; Wang, Y.; Li, J. The low-dimensional three-dimensional tin halide perovskite: Film characterization and device performance. *Energies* **2019**, *13*, 2. [CrossRef]
24. Chung, I.; Song, J.H.; Im, J.; Androulakis, J.; Malliakas, C.D.; Li, H.; Freeman, A.J.; Kenney, J.T.; Kanatzidis, M.G. CsSnI3: Semiconductor or metal? High electrical conductivity and strong near-infrared photoluminescence from a single material. High hole mobility and phase-transitions. *J. Am. Chem. Soc.* **2012**, *134*, 8579–8587. [CrossRef] [PubMed]
25. Wu, B.; Zhou, Y.; Xing, G.; Xu, Q.; Garces, H.F.; Solanki, A.; Goh, T.W.; Padture, N.P.; Sum, T.C. Long minority-carrier diffusion length and low surface-recombination velocity in inorganic lead-free CsSnI3 perovskite crystal for solar cells. *Adv. Funct. Mater.* **2017**, *27*, 1604818. [CrossRef]
26. Ma, L.; Hao, F.; Stoumpos, C.C.; Phelan, B.T.; Wasielewski, M.R.; Kanatzidis, M.G. Carrier Diffusion Lengths of over 500 nm in Lead-Free Perovskite CH3NH3SnI3 Films. *J. Am. Chem. Soc.* **2016**, *138*, 14750–14755. [CrossRef]

27. Shockley, W.; Queisser, H.J. Detailed Balance Limit of Efficiency of P-N Junction Solar Cells. *J. Appl. Phys.* **1961**, *32*, 510. [CrossRef]
28. Dixit, H.; Punetha, D.; Pandey, S.K. Improvement in performance of lead free inverted perovskite solar cell by optimization of solar parameters. *Optik* **2019**, *179*, 969–976. [CrossRef]
29. Song, Z.; Abate, A.; Watthage, S.C.; Liyanage, G.K.; Phillips, A.B.; Steiner, U.; Graetzel, M.; Heben, M.J. Perovskite solar cell stability in humid air: Partially reversible phase transitions in the PbI2-CH3NH3I-H2O system. *Adv. Energy Mater.* **2016**, *6*, 1600846. [CrossRef]
30. Mannino, G.; Alberti, A.; Deretzis, I.; Smecca, E.; Sanzaro, S.; Numata, Y.; Miyasaka, T.; La Magna, A. First evidence of CH3NH3PbI3 optical constants improvement in a N2 environment in the range 40–80 °C. *J. Phys. Chem. C* **2017**, *121*, 7703–7710. [CrossRef]
31. Bryant, D.; Aristidou, N.; Pont, S.; Sanchez-Molina, I.; Chotchunangatchaval, T.; Wheeler, S.; Durrant, J.R.; Haque, S.A. Light and oxygen induced degradation limits the operational stability of methylammonium lead triiodide perovskite solar cells. *Energy Environ. Sci.* **2016**, *9*, 1655–1660. [CrossRef]
32. Bae, S.; Kim, S.; Lee, S.-W.; Cho, K.J.; Park, S.; Lee, S.; Kang, Y.; Lee, H.-S.; Kim, D. Electric-field-induced degradation of methylammonium lead iodide perovskite solar cells. *J. Phys. Chem. Lett.* **2016**, *7*, 3091–3096. [CrossRef] [PubMed]
33. Alberti, A.; Deretzis, I.; Mannino, G.; Smecca, E.; Sanzaro, S.; Numata, Y.; Miyasaka, T.; La Magna, A. Revealing a discontinuity in the degradation behavior of CH3NH3PbI3 during thermal operation. *J. Phys. Chem. C* **2017**, *121*, 13577–13585. [CrossRef]
34. Zhao, T.; Chueh, C.-C.; Chen, Q.; Rajagopal, A.; Jen, A.K.-Y. Defect passivation of organic–inorganic hybrid perovskites by diammonium iodide toward high-performance photovoltaic devices. *ACS Energy Lett.* **2016**, *1*, 757–763. [CrossRef]
35. Ogomi, Y.; Morita, A.; Tsukamoto, S.; Saitho, T.; Fujikawa, N.; Shen, Q.; Toyoda, T.; Yoshino, K.; Pandey, S.S.; Ma, T. CH3NH3Sn x Pb (1−x) I3 Perovskite solar cells covering up to 1060 nm. *J. Phys. Chem. Lett.* **2014**, *5*, 1004–1011. [CrossRef]
36. Abate, A. Perovskite Solar Cells Go Lead Free. *Joule* **2017**, *1*, 659–664. [CrossRef]
37. Ke, W.; Kanatzidis, M.G. Prospects for low-toxicity lead-free perovskite solar cells. *Nat. Commun.* **2019**, *10*, 965. [CrossRef]
38. Lee, D.-Y.; Na, S.-I.; Kim, S.-S. Graphene oxide/PEDOT: PSS composite hole transport layer for efficient and stable planar heterojunction perovskite solar cells. *Nanoscale* **2016**, *8*, 1513–1522. [CrossRef]
39. Yamada, K.; Matsui, T.; Tsuritani, T.; Okuda, T.; Ichiba, S. 127I-NQR, 119 Sn Mössbauer effect, and electrical conductivity of MSnI3 (M= K, NH4, Rb, Cs, and CH3NH3). *Z. Nat. A* **1990**, *45*, 307–312. [CrossRef]
40. Stoumpos, C.C.; Malliakas, C.D.; Kanatzidis, M.G. Semiconducting tin and lead iodide perovskites with organic cations: Phase transitions, high mobilities, and near-infrared photoluminescent properties. *Inorg. Chem.* **2013**, *52*, 9019–9038. [CrossRef]
41. Fang, H.H.; Adjokatse, S.; Shao, S.; Even, J.; Loi, M.A. Long-lived hot-carrier light emission and large blue shift in formamidinium tin triiodide perovskites. *Nat. Commun.* **2018**, *9*, 243. [CrossRef] [PubMed]
42. Hao, F.; Stoumpos, C.C.; Guo, P.; Zhou, N.; Marks, T.J.; Chang, R.P.; Kanatzidis, M.G. Solvent-mediated crystallization of CH3NH3SnI3 films for heterojunction depleted perovskite solar cells. *J. Am. Chem. Soc.* **2015**, *137*, 11445–11452. [CrossRef] [PubMed]
43. Mitzi, D.B.; Feild, C.A.; Harrison, W.T.A.; Guloy, A.M. Conducting Tin Halides with a Layered Organic-Based Perovskite Structure. *Nature* **1994**, *369*, 467–469. [CrossRef]
44. Mitzi, D.; Wang, S.; Feild, C.; Chess, C.; Guloy, A. Conducting layered organic-inorganic halides containing <110>-oriented perovskite sheets. *Science* **1995**, *267*, 1473–1476. [CrossRef] [PubMed]
45. Mitzi, D.B.; Feild, C.A.; Schlesinger, Z.; Laibowitz, R.B. Transport, Optical, and Magnetic Properties of the Conducting Halide Perovskite CH3NH3SnI3. *J. Solid State Chem.* **1995**, *114*, 159–163. [CrossRef]
46. Mitzi, D.B.; Liang, K. Synthesis, Resistivity, and Thermal Properties of the Cubic Perovskite NH2CH=NH2SnI3and Related Systems. *J. Solid State Chem.* **1997**, *134*, 376–381. [CrossRef]
47. Li, X.T.; Wu, J.B.; Wang, S.H.; Qi, Y.B. Progress of All-inorganic Cesium Lead-free Perovskite Solar Cells. *Chem. Lett.* **2019**, *48*, 989–1005. [CrossRef]
48. Li, B.; Chang, B.; Pan, L.; Li, Z.; Fu, L.; He, Z.; Yin, L. Tin-based defects and passivation strategies in tin-related perovskite solar cells. *ACS Energy Lett.* **2020**, *5*, 3752–3772. [CrossRef]
49. Umari, P.; Mosconi, E.; De Angelis, F. Relativistic GW calculations on CH3NH3PbI3 and CH3NH3SnI3 perovskites for solar cell applications. *Sci. Rep.* **2014**, *4*, 4467. [CrossRef]
50. Cox, H.; Stace, A.J. Molecular View of the Anomalous Acidities of Sn2+, Pb2+, and Hg2+. *J. Am. Chem. Soc.* **2004**, *126*, 3939–3947. [CrossRef]
51. LaMer, V.K.; Dinegar, R.H. Theory, Production and Mechanism of Formation of Monodispersed Hydrosols. *J. Am. Chem. Soc.* **1950**, *72*, 4847–4854. [CrossRef]
52. Chen, B.; Rudd, P.N.; Yang, S.; Yuan, Y.; Huang, J. Imperfections and their passivation in halide perovskite solar cells. *Chem. Soc. Rev.* **2019**, *48*, 3842–3867. [CrossRef] [PubMed]
53. Liao, W.; Zhao, D.; Yu, Y.; Grice, C.R.; Wang, C.; Cimaroli, A.J.; Schulz, P.; Meng, W.; Zhu, K.; Xiong, R.G. Lead-free inverted planar formamidinium tin triiodide perovskite solar cells achieving power conversion efficiencies up to 6.22%. *Adv. Mater.* **2016**, *28*, 9333–9340. [CrossRef] [PubMed]
54. Hao, F.; Stoumpos, C.C.; Chang, R.P.; Kanatzidis, M.G. Anomalous band gap behavior in mixed Sn and Pb perovskites enables broadening of absorption spectrum in solar cells. *J. Am. Chem. Soc.* **2014**, *136*, 8094–8099. [CrossRef]

55. Sun, N.; Gao, W.; Dong, H.; Liu, Y.; Liu, X.; Wu, Z.; Song, L.; Ran, C.; Chen, Y. Architecture of p-i-n Sn-Based Perovskite Solar Cells: Characteristics, Advances, and Perspectives. *ACS Energy Lett.* **2021**, *6*, 2863–2875. [CrossRef]
56. Kuan, C.-H.; Luo, G.-S.; Narra, S.; Maity, S.; Hiramatsu, H.; Tsai, Y.-W.; Lin, J.-M.; Hou, C.-H.; Shyue, J.-J.; Wei-Guang Diau, E. How can a hydrophobic polymer PTAA serve as a hole- transport layer for an inverted tin perovskite solar cell? *Chem. Eng. J.* **2022**, *450*, 138037. [CrossRef]
57. Ke, W.; Stoumpos, C.C.; Kanatzidis, M.G. "Unleaded" Perovskites: Status Quo and Future Prospects of Tin-Based Perovskite Solar Cells. *Adv. Mater.* **2019**, *31*, e1803230. [CrossRef]
58. Awais, M.; Kirsch, R.L.; Yeddu, V.; Saidaminov, M.I. Tin Halide Perovskites Going Forward: Frost Diagrams Offer Hints. *ACS Mater. Lett.* **2021**, *3*, 299–307. [CrossRef]
59. Aftab, A.; Ahmad, M.I. A review of stability and progress in tin halide perovskite solar cell. *Sol. Energy* **2021**, *216*, 26–47. [CrossRef]
60. Song, T.-B.; Yokoyama, T.; Stoumpos, C.C.; Logsdon, J.; Cao, D.H.; Wasielewski, M.R.; Aramaki, S.; Kanatzidis, M.G. Importance of reducing vapor atmosphere in the fabrication of tin-based perovskite solar cells. *J. Am. Chem. Soc.* **2017**, *139*, 836–842. [CrossRef]
61. Christians, J.A.; Miranda Herrera, P.A.; Kamat, P.V. Transformation of the excited state and photovoltaic efficiency of CH3NH3PbI3 perovskite upon controlled exposure to humidified air. *J. Am. Chem. Soc.* **2015**, *137*, 1530–1538. [CrossRef] [PubMed]
62. Niu, G.D.; Guo, X.D.; Wang, L.D. Review of recent progress in chemical stability of perovskite solar cells. *J. Mater. Chem. A* **2015**, *3*, 8970–8980. [CrossRef]
63. Wang, F.; Ma, J.; Xie, F.; Li, L.; Chen, J.; Fan, J.; Zhao, N. Organic Cation-Dependent Degradation Mechanism of Organotin Halide Perovskites. *Adv. Funct. Mater.* **2016**, *26*, 3417–3423. [CrossRef]
64. Wang, K.; Liang, Z.; Wang, X.; Cui, X. Lead replacement in CH3NH3PbI3 perovskites. *Adv. Electron. Mater.* **2015**, *1*, 1500089. [CrossRef]
65. Lanzetta, L.; Webb, T.; Zibouche, N.; Liang, X.; Ding, D.; Min, G.; Westbrook, R.J.; Gaggio, B.; Macdonald, T.J.; Islam, M.S. Degradation mechanism of hybrid tin-based perovskite solar cells and the critical role of tin (IV) iodide. *Nat. Commun.* **2021**, *12*, 2853. [CrossRef] [PubMed]
66. Wang, S.H.; Jiang, Y.; Juarez-Perez, E.J.; Ono, L.K.; Qi, Y.B. Accelerated degradation of methylammonium lead iodide perovskites induced by exposure to iodine vapour. *Nat. Energy* **2017**, *2*, 16195. [CrossRef]
67. Leijtens, T.; Eperon, G.E.; Pathak, S.; Abate, A.; Lee, M.M.; Snaith, H.J. Overcoming ultraviolet light instability of sensitized TiO2 with meso-superstructured organometal tri-halide perovskite solar cells. *Nat. Commun.* **2013**, *4*, 2885. [CrossRef] [PubMed]
68. Lee, M.M.; Teuscher, J.; Miyasaka, T.; Murakami, T.N.; Snaith, H.J. Efficient hybrid solar cells based on meso-superstructured organometal halide perovskites. *Science* **2012**, *338*, 643–647. [CrossRef]
69. Wang, C.; Zhang, Y.; Gu, F.; Zhao, Z.; Li, H.; Jiang, H.; Bian, Z.; Liu, Z. Illumination Durability and High-Efficiency Sn-Based Perovskite Solar Cell under Coordinated Control of Phenylhydrazine and Halogen Ions. *Matter* **2021**, *4*, 709–721. [CrossRef]
70. Juarez-Perez, E.J.; Ono, L.K.; Maeda, M.; Jiang, Y.; Hawash, Z.; Qi, Y. Photodecomposition and thermal decomposition in methylammonium halide lead perovskites and inferred design principles to increase photovoltaic device stability. *J. Mater. Chem. A* **2018**, *6*, 9604. [CrossRef]
71. Juarez-Perez, E.J.; Hawash, Z.; Raga, S.R.; Ono, L.K.; Qi, Y. Thermal degradation of CH3NH3PbI3 perovskite into NH3 and CH3I gases observed by coupled thermogravimetry–mass spectrometry analysis. *Energy Environ. Sci.* **2016**, *9*, 3406. [CrossRef]
72. Xu, L.; Feng, X.; Jia, W.; Lv, W.; Mei, A.; Zhou, Y.; Zhang, Q.; Chen, R.; Huang, W. Recent advances and challenges of inverted lead-free tin-based perovskite solar cells. *Energy Environ. Sci.* **2021**, *14*, 4292–4317. [CrossRef]
73. Chen, B.; Yang, M.; Zheng, X.; Wu, C.; Li, W.; Yan, Y.; Bisquert, J.; Garcia-Belmonte, G.; Zhu, K.; Priya, S. Impact of capacitive effect and ion migration on the hysteretic behavior of perovskite solar cells. *J. Phys. Chem. Lett.* **2015**, *6*, 4693–4700. [CrossRef] [PubMed]
74. Mosconi, E.; Umari, P.; De Angelis, F. Electronic and optical properties of mixed Sn–Pb organohalide perovskites: A first principles investigation. *J. Mater. Chem. A* **2015**, *3*, 9208–9215. [CrossRef]
75. Li, S.; Liu, P.; Pan, L.; Li, W.; Yang, S.-E.; Shi, Z.; Guo, H.; Xia, T.; Zhang, S.; Chen, Y. The investigation of inverted pin planar perovskite solar cells based on FASnI3 films. *Sol. Energy Mater. Sol. Cells* **2019**, *199*, 75–82. [CrossRef]
76. Lee, H.; Lee, C.; Song, H.-J. Influence of electrical traps on the current density degradation of inverted perovskite solar cells. *Materials* **2019**, *12*, 1644. [CrossRef]
77. Meng, X.; Lin, J.; Liu, X.; He, X.; Wang, Y.; Noda, T.; Wu, T.; Yang, X.; Han, L. Highly Stable and Efficient FASnI3-Based Perovskite Solar Cells by Introducing Hydrogen Bonding. *Adv. Mater.* **2019**, *31*, 1903721. [CrossRef]
78. Okuya, M.; Prokudina, N.A.; Mushika, K.; Kaneko, S. TiO2 thin films synthesized by the spray pyrolysis deposition (SPD) technique. *J. Eur. Ceram. Soc.* **1999**, *19*, 903–906. [CrossRef]
79. Tiwana, P.; Docampo, P.; Johnston, M.B.; Snaith, H.J.; Herz, L.M. Electron mobility and injection dynamics in mesoporous ZnO, SnO2, and TiO2 films used in dye-sensitized solar cells. *ACS Nano* **2011**, *5*, 5158–5166. [CrossRef]
80. Heo, J.H.; Lee, M.H.; Han, H.J.; Patil, B.R.; Yu, J.S.; Im, S.H. Highly efficient low temperature solution processable planar type CH 3 NH 3 PbI 3 perovskite flexible solar cells. *J. Mater. Chem. A* **2016**, *4*, 1572–1578. [CrossRef]
81. Qiu, L.; Liu, Z.; Ono, L.K.; Jiang, Y.; Son, D.Y.; Hawash, Z.; He, S.; Qi, Y. Scalable Fabrication of Stable High Efficiency Perovskite Solar Cells and Modules Utilizing Room Temperature Sputtered SnO2 Electron Transport Layer. *Adv. Funct. Mater.* **2019**, *29*, 1806779. [CrossRef]

82. Jiang, Q.; Zhang, X.; You, J. SnO2: A wonderful electron transport layer for perovskite solar cells. *Small* **2018**, *14*, 1801154. [CrossRef] [PubMed]
83. Huang, L.; Sun, X.; Li, C.; Xu, J.; Xu, R.; Du, Y.; Ni, J.; Cai, H.; Li, J.; Hu, Z. UV-sintered low-temperature solution-processed SnO2 as robust electron transport layer for efficient planar heterojunction perovskite solar cells. *ACS Appl. Mater. Interfaces* **2017**, *9*, 21909–21920. [CrossRef] [PubMed]
84. Noh, M.F.M.; Soh, M.F.; Teh, C.H.; Lim, E.L.; Yap, C.C.; Ibrahim, M.A.; Ludin, N.A.; Teridi, M.A.M. Effect of temperature on the properties of SnO2 layer fabricated via AACVD and its application in photoelectrochemical cells and organic photovoltaic devices. *Sol. Energy* **2017**, *158*, 474–482. [CrossRef]
85. Zhu, Z.; Chueh, C.C.; Li, N.; Mao, C.; Jen, A.K.Y. Realizing efficient lead-free formamidinium tin triiodide perovskite solar cells via a sequential deposition route. *Adv. Mater.* **2018**, *30*, 1703800. [CrossRef]
86. Zahran, R.; Hawash, Z. Fullerene-Based Inverted Perovskite Solar Cell: A Key to Achieve Promising, Stable, and Efficient Photovoltaics. *Adv. Mater. Interfaces* **2022**, *9*, 2201438. [CrossRef]
87. Ryu, S.; Seo, J.; Shin, S.S.; Kim, Y.C.; Jeon, N.J.; Noh, J.H.; Seok, S.I. Fabrication of metal-oxide-free CH 3 NH 3 PbI 3 perovskite solar cells processed at low temperature. *J. Mater. Chem. A* **2015**, *3*, 3271–3275. [CrossRef]
88. Fang, Y.; Bi, C.; Wang, D.; Huang, J. The Functions of Fullerenes in Hybrid Perovskite Solar Cells. *ACS Energy Lett.* **2017**, *2*, 782–794. [CrossRef]
89. Hawash, Z.; Ono, L.K.; Qi, Y.B. Recent Advances in Spiro-MeOTAD Hole Transport Material and Its Applications in Organic-Inorganic Halide Perovskite Solar Cells. *Adv. Mater. Interfaces* **2018**, *5*, 1700623. [CrossRef]
90. Meng, L.; You, J.; Guo, T.F.; Yang, Y. Recent Advances in the Inverted Planar Structure of Perovskite Solar Cells. *Acc. Chem. Res.* **2016**, *49*, 155–165. [CrossRef]
91. Zhang, X.; Qiu, W.; Song, W.; Hawash, Z.; Wang, Y.; Pradhan, B.; Zhang, Y.; Naumenko, D.; Amenitsch, H.; Moons, E.; et al. An Integrated Bulk and Surface Modification Strategy for Gas-Quenched Inverted Perovskite Solar Cells with Efficiencies Exceeding 22%. *Sol. RRL* **2022**, *6*, 2200053. [CrossRef]
92. Jeng, J.-Y.; Chiang, Y.-F.; Lee, M.-H.; Peng, S.-R.; Guo, T.-F.; Chen, P.; Wen, T.-C. CH3NH3PbI3 Perovskite/Fullerene Planar-Heterojunction Hybrid Solar Cells. *Adv. Mater.* **2013**, *25*, 3727–3732. [CrossRef] [PubMed]
93. Wang, Z.-K.; Li, M.; Yuan, D.-X.; Shi, X.-B.; Ma, H.; Liao, L.-S. Improved Hole Interfacial Layer for Planar Perovskite Solar Cells with Efficiency Exceeding 15%. *ACS Appl. Mater. Interfaces* **2015**, *7*, 9645–9651. [CrossRef]
94. Susic, I.; Zanoni, K.P.S.; Paliwal, A.; Kaya, I.C.; Hawash, Z.; Sessolo, M.; Moons, E.; Bolink, H.J. Intrinsic Organic Semiconductors as Hole Transport Layers in p–i–n Perovskite Solar Cells. *Sol. RRL* **2022**, *6*, 2100882. [CrossRef]
95. Leijtens, T.; Prasanna, R.; Gold-Parker, A.; Toney, M.F.; McGehee, M.D. Mechanism of Tin Oxidation and Stabilization by Lead Substitution in Tin Halide Perovskites. *ACS Energy Lett.* **2017**, *2*, 2159–2165. [CrossRef]
96. Hawash, Z.; Ono, L.K.; Qi, Y. Moisture and Oxygen Enhance Conductivity of LiTFSI-Doped Spiro-MeOTAD Hole Transport Layer in Perovskite Solar Cells. *Adv. Mater. Interfaces* **2016**, *3*, 1600117. [CrossRef]
97. Juarez-Perez, E.J.; Leyden, M.R.; Wang, S.H.; Ono, L.K.; Hawash, Z.; Qi, Y.B. Role of the Dopants on the Morphological and Transport Properties of Spiro-MeOTAD Hole Transport Layer. *Chem. Mater.* **2016**, *28*, 5702–5709. [CrossRef]
98. Calado, P.; Telford, A.M.; Bryant, D.; Li, X.; Nelson, J.; O'Regan, B.C.; Barnes, P.R. Evidence for ion migration in hybrid perovskite solar cells with minimal hysteresis. *Nat. Commun.* **2016**, *7*, 13831. [CrossRef]
99. Hawash, Z.; Ono, L.K.; Raga, S.R.; Lee, M.V.; Qi, Y. Air-Exposure Induced Dopant Redistribution and Energy Level Shifts in Spin-Coated Spiro-MeOTAD Films. *Chem. Mater.* **2015**, *27*, 562. [CrossRef]
100. Yu, B.B.; Xu, L.; Liao, M.; Wu, Y.; Liu, F.; He, Z.; Ding, J.; Chen, W.; Tu, B.; Lin, Y. Synergy Effect of Both 2, 2, 2-Trifluoroethylamine Hydrochloride and SnF2 for Highly Stable FASnI3− xClx Perovskite Solar Cells. *Sol. RRL* **2019**, *3*, 1800290. [CrossRef]
101. Cao, J.; Tai, Q.; You, P.; Tang, G.; Wang, T.; Wang, N.; Yan, F. Enhanced performance of tin-based perovskite solar cells induced by an ammonium hypophosphite additive. *J. Mater. Chem. A* **2019**, *7*, 26580–26585. [CrossRef]
102. Yin, X.; Guo, Y.; Xie, H.; Que, W.; Kong, L.B. Nickel oxide as efficient hole transport materials for perovskite solar cells. *Sol. RRL* **2019**, *3*, 1900001. [CrossRef]
103. Lee, S.J.; Shin, S.S.; Kim, Y.C.; Kim, D.; Ahn, T.K.; Noh, J.H.; Seo, J.; Seok, S.I. Fabrication of efficient formamidinium tin iodide perovskite solar cells through SnF2–pyrazine complex. *J. Am. Chem. Soc.* **2016**, *138*, 3974–3977. [CrossRef] [PubMed]
104. Milot, R.L.; Klug, M.T.; Davies, C.L.; Wang, Z.; Kraus, H.; Snaith, H.J.; Johnston, M.B.; Herz, L.M. The effects of doping density and temperature on the optoelectronic properties of formamidinium tin triiodide thin films. *Adv. Mater.* **2018**, *30*, 1804506. [CrossRef] [PubMed]
105. Kumar, M.H.; Dharani, S.; Leong, W.L.; Boix, P.P.; Prabhakar, R.R.; Baikie, T.; Shi, C.; Ding, H.; Ramesh, R.; Asta, M. Lead-free halide perovskite solar cells with high photocurrents realized through vacancy modulation. *Adv. Mater.* **2014**, *26*, 7122–7127. [CrossRef] [PubMed]
106. Xiao, M.; Gu, S.; Zhu, P.C.; Tang, M.Y.; Zhu, W.D.; Lin, R.X.; Chen, C.L.; Xu, W.C.; Yu, T.; Zhu, J. Tin-Based Perovskite with Improved Coverage and Crystallinity through Tin-Fluoride-Assisted Heterogeneous Nucleation. *Adv. Opt. Mater.* **2018**, *6*, 1700615. [CrossRef]
107. Hartmann, C.; Gupta, S.; Bendikov, T.; Kozina, X.; Kunze, T.; Felix, R.; Hodes, G.; Wilks, R.G.; Cahen, D.; Bar, M. Impact of SnF2 Addition on the Chemical and Electronic Surface Structure of CsSnBr3. *ACS Appl. Mater. Interfaces* **2020**, *12*, 12353–12361. [CrossRef]

108. Marshall, K.; Walker, M.; Walton, R.; Hatton, R. Enhanced stability and efficiency in hole-transport-layer-free CsSnI3 perovskite photovoltaics. *Nat. Energy* **2016**, *1*, 16178. [CrossRef]
109. Kayesh, M.E.; Chowdhury, T.H.; Matsuishi, K.; Kaneko, R.; Kazaoui, S.; Lee, J.-J.; Noda, T.; Islam, A. Enhanced photovoltaic performance of FASnI3-based perovskite solar cells with hydrazinium chloride coadditive. *ACS Energy Lett.* **2018**, *3*, 1584–1589. [CrossRef]
110. Li, F.; Zhang, C.; Huang, J.H.; Fan, H.; Wang, H.; Wang, P.; Zhan, C.; Liu, C.M.; Li, X.; Yang, L.M. A Cation-Exchange Approach for the Fabrication of Efficient Methylammonium Tin Iodide Perovskite Solar Cells. *Angew. Chem. Int. Ed.* **2019**, *58*, 6688–6692. [CrossRef]
111. Li, W.; Li, J.; Li, J.; Fan, J.; Mai, Y.; Wang, L. Addictive-assisted construction of all-inorganic CsSnIBr 2 mesoscopic perovskite solar cells with superior thermal stability up to 473 K. *J. Mater. Chem. A* **2016**, *4*, 17104–17110. [CrossRef]
112. Wang, T.; Tai, Q.; Guo, X.; Cao, J.; Liu, C.-K.; Wang, N.; Shen, D.; Zhu, Y.; Lee, C.-S.; Yan, F. Highly air-stable tin-based perovskite solar cells through grain-surface protection by gallic acid. *ACS Energy Lett.* **2020**, *5*, 1741–1749. [CrossRef]
113. Xu, X.; Chueh, C.-C.; Yang, Z.; Rajagopal, A.; Xu, J.; Jo, S.B.; Jen, A.K.-Y. Ascorbic acid as an effective antioxidant additive to enhance the efficiency and stability of Pb/Sn-based binary perovskite solar cells. *Nano Energy* **2017**, *34*, 392–398. [CrossRef]
114. Choi, J.I.J.; Khan, M.E.; Hawash, Z.; Lee, H.; Ono, L.K.; Qi, Y.; Kim, Y.-H.; Park, J.Y. Surface Termination-Dependent Nanotribological Properties of Single-Crystal MAPbBr3 Surfaces. *J. Phys. Chem. C* **2020**, *124*, 1484–1491. [CrossRef]
115. Hawash, Z.; Raga, S.R.; Son, D.Y.; Ono, L.K.; Park, N.G.; Qi, Y. Interfacial Modification of Perovskite Solar Cells Using an Ultrathin MAI Layer Leads to Enhanced Energy Level Alignment, Efficiencies, and Reproducibility. *J. Phys. Chem. Lett.* **2017**, *8*, 3947. [CrossRef] [PubMed]
116. He, X.; Wu, T.; Liu, X.; Wang, Y.; Meng, X.; Wu, J.; Noda, T.; Yang, X.; Moritomo, Y.; Segawa, H. Highly efficient tin perovskite solar cells achieved in a wide oxygen concentration range. *J. Mater. Chem. A* **2020**, *8*, 2760–2768. [CrossRef]
117. Guarnera, S.; Abate, A.; Zhang, W.; Foster, J.M.; Richardson, G.; Petrozza, A.; Snaith, H.J. Improving the long-term stability of perovskite solar cells with a porous Al2O3 buffer layer. *J. Phys. Chem. Lett.* **2015**, *6*, 432–437. [CrossRef]
118. Chang, C.-Y.; Huang, W.-K.; Wu, J.-L.; Chang, Y.-C.; Lee, K.-T.; Chen, C.-T. Room-temperature solution-processed n-doped zirconium oxide cathode buffer layer for efficient and stable organic and hybrid perovskite solar cells. *Chem. Mater.* **2016**, *28*, 242–251. [CrossRef]
119. Nishimura, K.; Hirotani, D.; Kamarudin, M.A.; Shen, Q.; Toyoda, T.; Iikubo, S.; Minemoto, T.; Yoshino, K.; Hayase, S. Relationship between lattice strain and efficiency for Sn-perovskite solar cells. *ACS Appl. Mater. Interfaces* **2019**, *11*, 31105–31110. [CrossRef]
120. Sun, N.; Gao, W.; Dong, H.; Liu, X.; Chao, L.; Hui, W.; Xia, Y.; Ran, C.; Chen, Y. Bi-Linkable Reductive Cation as Molecular Glue for One Year Stable Sn-Based Perovskite Solar Cells. *ACS Appl. Energy Mater.* **2022**, *5*, 4008–4016. [CrossRef]
121. Ono, L.K.; Hawash, Z.; Juarez-Perez, E.J.; Qiu, L.B.; Jiang, Y.; Qi, Y.B. The influence of secondary solvents on the morphology of a spiro-MeOTAD hole transport layer for lead halide perovskite solar cells. *J. Phys. D Appl. Phys.* **2018**, *51*, 294001. [CrossRef]
122. Liu, C.; Fan, J.; Li, H.; Zhang, C.; Mai, Y. Highly Efficient Perovskite Solar Cells with Substantial Reduction of Lead Content. *Sci. Rep.* **2016**, *6*, 35705. [CrossRef] [PubMed]
123. Liu, X.H.; Yan, K.; Tan, D.W.; Liang, X.; Zhang, H.M.; Huang, W. Solvent Engineering Improves Efficiency of Lead-Free Tin-Based Hybrid Perovskite Solar Cells beyond 9%. *ACS Energy Lett.* **2018**, *3*, 2701–2707. [CrossRef]
124. Liu, J.; Ozaki, M.; Yakumaru, S.; Handa, T.; Nishikubo, R.; Kanemitsu, Y.; Saeki, A.; Murata, Y.; Murdey, R.; Wakamiya, A. Lead-Free Solar Cells based on Tin Halide Perovskite Films with High Coverage and Improved Aggregation. *Angew. Chem.* **2018**, *130*, 13405–13409. [CrossRef]
125. Liu, G.; Liu, C.; Lin, Z.; Yang, J.; Huang, Z.; Tan, L.; Chen, Y. Regulated crystallization of efficient and stable tin-based perovskite solar cells via a self-sealing polymer. *ACS Appl. Mater. Interfaces* **2020**, *12*, 14049–14056. [CrossRef] [PubMed]
126. Luo, S.-Q.; Wang, J.-F.; Yang, B.; Yuan, Y.-B. Recent advances in controlling the crystallization of two-dimensional perovskites for optoelectronic device. *Front. Phys.* **2019**, *14*, 53401. [CrossRef]
127. Stoumpos, C.C.; Cao, D.H.; Clark, D.J.; Young, J.; Rondinelli, J.M.; Jang, J.I.; Hupp, J.T.; Kanatzidis, M.G. Ruddlesden–Popper hybrid lead iodide perovskite 2D homologous semiconductors. *Chem. Mater.* **2016**, *28*, 2852–2867. [CrossRef]
128. You, P.; Tang, G.; Cao, J.; Shen, D.; Ng, T.W.; Hawash, Z.; Wang, N.; Liu, C.K.; Lu, W.; Tai, Q.; et al. 2D materials for conducting holes from grain boundaries in perovskite solar cells. *Light Sci. Appl.* **2021**, *10*, 68. [CrossRef]
129. Cao, D.H.; Stoumpos, C.C.; Farha, O.K.; Hupp, J.T.; Kanatzidis, M.G. 2D homologous perovskites as light-absorbing materials for solar cell applications. *J. Am. Chem. Soc.* **2015**, *137*, 7843–7850. [CrossRef]
130. Smith, I.C.; Hoke, E.T.; Solis-Ibarra, D.; McGehee, M.D.; Karunadasa, H.I. A layered hybrid perovskite solar-cell absorber with enhanced moisture stability. *Angew. Chem. Int. Ed.* **2014**, *53*, 11232–11235. [CrossRef]
131. Lin, Y.; Bai, Y.; Fang, Y.; Wang, Q.; Deng, Y.; Huang, J. Suppressed ion migration in low-dimensional perovskites. *ACS Energy Lett.* **2017**, *2*, 1571–1572. [CrossRef]
132. Peng, W.; Yin, J.; Ho, K.-T.; Ouellette, O.; De Bastiani, M.; Murali, B.; El Tall, O.; Shen, C.; Miao, X.; Pan, J. Ultralow self-doping in two-dimensional hybrid perovskite single crystals. *Nano Lett.* **2017**, *17*, 4759–4767. [CrossRef] [PubMed]
133. Liao, Y.; Liu, H.; Zhou, W.; Yang, D.; Shang, Y.; Shi, Z.; Li, B.; Jiang, X.; Zhang, L.; Quan, L.N. Highly oriented low-dimensional tin halide perovskites with enhanced stability and photovoltaic performance. *J. Am. Chem. Soc.* **2017**, *139*, 6693–6699. [CrossRef]
134. Jiang, X.; Wang, F.; Wei, Q.; Li, H.; Shang, Y.; Zhou, W.; Wang, C.; Cheng, P.; Chen, Q.; Chen, L. Ultra-high open-circuit voltage of tin perovskite solar cells via an electron transporting layer design. *Nat. Commun.* **2020**, *11*, 1245. [CrossRef] [PubMed]

135. Zhang, M.; Zhang, Z.; Cao, H.; Zhang, T.; Yu, H.; Du, J.; Shen, Y.; Zhang, X.-L.; Zhu, J.; Chen, P.; et al. Recent progress in inorganic tin perovskite solar cells. *Mater. Today Energy* **2022**, *23*, 100891. [CrossRef]
136. Jeon, I.; Kim, K.; Jokar, E.; Park, M.; Lee, H.-W.; Diau, E.W.-G. Environmentally Compatible Lead-Free Perovskite Solar Cells and Their Potential as Light Harvesters in Energy Storage Systems. *Nanomaterials* **2021**, *11*, 2066. [CrossRef] [PubMed]
137. Cao, J.; Yan, F. Recent progress in tin-based perovskite solar cells. *Energy Environ. Sci.* **2021**, *14*, 1286–1325. [CrossRef]
138. Yang, S.J.; Choi, J.; Song, S.; Park, C.; Cho, K. Enhancing air-stability and reproducibility of lead-free formamidinium-based tin perovskite solar cell by chlorine doping. *Sol. Energy Mater. Sol. Cells* **2021**, *227*, 111072. [CrossRef]
139. Ye, T.; Wang, K.; Hou, Y.; Yang, D.; Smith, N.; Magill, B.; Yoon, J.; Mudiyanselage, R.; Khodaparast, G.A.; Wang, K.; et al. Ambient-Air-Stable Lead-Free CsSnI3 Solar Cells with Greater than 7.5% Efficiency. *J. Am. Chem. Soc.* **2021**, *143*, 4319–4328. [CrossRef]
140. Mahmoudi, T.; Rho, W.-Y.; Kohan, M.; Im, Y.H.; Mathur, S.; Hahn, Y.-B. Suppression of Sn2+/Sn4+ oxidation in tin-based perovskite solar cells with graphene-tin quantum dots composites in active layer. *Nano Energy* **2021**, *90*, 106495. [CrossRef]
141. Cho, S.; Pandey, P.; Park, J.; Lee, T.-W.; Ahn, H.; Choi, H.; Kang, D.-W. Phenylethylammonium-formamidinium-methylammonium quasi-2D/3D tin wide-bandgap perovskite solar cell with improved efficiency and stability. *Chem. Eng. J.* **2022**, *446*, 137388. [CrossRef]
142. Yang, J.; Sheng, W.; Xiao, S.; Liu, G.; Lin, Z.; Tan, L.; Chen, Y. Directional Crystallization by Floating Self-Assembly for Efficient and Stable Tin-based Perovskite Solar Cells. *Chem. Mater.* **2021**, *33*, 4362–4372. [CrossRef]
143. Ji, L.; Zhang, T.; Wang, Y.; Liu, D.; Chen, H.; Zheng, H.; Peng, X.; Yuan, S.; Chen, Z.D.; Li, S. Regulating crystallization dynamics and crystal orientation of methylammonium tin iodide enables high-efficiency lead-free perovskite solar cells. *Nanoscale* **2022**, *14*, 1219–1225. [CrossRef]
144. Xu, R.; Dong, H.; Li, P.; Cao, X.; Li, H.; Li, J.; Wu, Z. Formamidine Acetate Induces Regulation of Crystallization and Stabilization in Sn-Based Perovskite Solar Cells. *ACS Appl. Mater. Interfaces* **2021**, *13*, 33218–33225. [CrossRef]
145. Chen, M.; Dong, Q.; Xiao, C.; Zheng, X.; Dai, Z.; Shi, Y.; Luther, J.M.; Padture, N.P. Lead-Free Flexible Perovskite Solar Cells with Interfacial Native Oxide Have >10% Efficiency and Simultaneously Enhanced Stability and Reliability. *ACS Energy Lett.* **2022**, *7*, 2256–2264. [CrossRef]
146. Sanchez-Diaz, J.; Sánchez, R.S.; Masi, S.; Krečmarová, M.; Alvarez, A.O.; Barea, E.M.; Rodriguez-Romero, J.; Chirvony, V.S.; Sánchez-Royo, J.F.; Martinez-Pastor, J.P.; et al. Tin perovskite solar cells with >1300 h of operational stability in N_2 through a synergistic chemical engineering approach. *Joule* **2022**, *6*, 861–883. [CrossRef]
147. Chen, Y.; Wang, K.; Qi, H.; Zhang, Y.; Wang, T.; Tong, Y.; Wang, H. Mitigating Voc Loss in Tin Perovskite Solar Cells via Simultaneous Suppression of Bulk and Interface Nonradiative Recombination. *ACS Appl. Mater. Interfaces* **2022**, *14*, 41086–41094. [CrossRef]
148. Cui, D.; Liu, X.; Wu, T.; Lin, X.; Luo, X.; Wu, Y.; Segawa, H.; Yang, X.; Zhang, Y.; Wang, Y.; et al. Making Room for Growing Oriented FASnI3 with Large Grains via Cold Precursor Solution. *Adv. Funct. Mater.* **2021**, *31*, 2100931. [CrossRef]
149. Qin, M.; Li, Y.; Yang, Y.; Chan, P.F.; Li, S.; Qin, Z.; Guo, X.; Shu, L.; Zhu, Y.; Fan, Z.; et al. Regulating the Crystallization Kinetics and Lattice Strain of Lead-Free Perovskites with Perovskite Quantum Dots. *ACS Energy Lett.* **2022**, *7*, 3251–3259. [CrossRef]
150. Wang, S.; Yan, L.; Zhu, W.; Cao, Z.; Zhou, L.; Ding, L.; Hao, F. Suppressing the formation of tin vacancy yields efficient lead-free perovskite solar cells. *Nano Energy* **2022**, *99*, 107416. [CrossRef]
151. Liu, G.; Zhong, Y.; Feng, W.; Yang, M.; Yang, G.; Zhong, J.-X.; Tian, T.; Luo, J.-B.; Tao, J.; Yang, S. Multidentate Chelation Heals Structural Imperfections for Minimized Recombination Loss in Lead-Free Perovskite Solar Cells. *Angew. Chem.* **2022**, *134*, e202209464.
152. Zhu, Z.; Jiang, X.; Yu, D.; Yu, N.; Ning, Z.; Mi, Q. Smooth and Compact FASnI3 Films for Lead-Free Perovskite Solar Cells with over 14% Efficiency. *ACS Energy Lett.* **2022**, *7*, 2079–2083. [CrossRef]
153. Jiang, X.; Li, H.; Zhou, Q.; Wei, Q.; Wei, M.; Jiang, L.; Wang, Z.; Peng, Z.; Wang, F.; Zang, Z.; et al. One-Step Synthesis of SnI2·(DMSO)x Adducts for High-Performance Tin Perovskite Solar Cells. *J. Am. Chem. Soc.* **2021**, *143*, 10970–10976. [CrossRef] [PubMed]
154. Yu, B.B.; Chen, Z.; Zhu, Y.; Wang, Y.; Han, B.; Chen, G.; Zhang, X.; Du, Z.; He, Z. Heterogeneous 2D/3D tin-halides perovskite solar cells with certified conversion efficiency breaking 14%. *Adv. Mater.* **2021**, *33*, 2102055. [CrossRef] [PubMed]
155. Li, B.; Di, H.; Chang, B.; Yin, R.; Fu, L.; Zhang, Y.-N.; Yin, L. Efficient Passivation Strategy on Sn Related Defects for High Performance All-Inorganic CsSnI3 Perovskite Solar Cells. *Adv. Funct. Mater.* **2021**, *31*, 2007447. [CrossRef]
156. Chen, M.; Kapil, G.; Wang, L.; Razey Sahamir, S.; Baranwal, A.K.; Nishimura, K.; Sanehira, Y.; Zhang, Z.; Akmal Kamarudin, M.; Shen, Q.; et al. High performance wide bandgap Lead-free perovskite solar cells by monolayer engineering. *Chem. Eng. J.* **2022**, *436*, 135196. [CrossRef]
157. Hu, M.; Nie, R.; Kim, H.; Wu, J.; Chen, S.; Park, B.-w.; Kim, G.; Kwon, H.-W.; Seok, S.I. Regulating the Surface Passivation and Residual Strain in Pure Tin Perovskite Films. *ACS Energy Lett.* **2021**, *6*, 3555–3562. [CrossRef]
158. Li, F.; Hou, X.; Wang, Z.; Cui, X.; Xie, G.; Yan, F.; Zhao, X.-Z.; Tai, Q. FA/MA Cation Exchange for Efficient and Reproducible Tin-Based Perovskite Solar Cells. *ACS Appl. Mater. Interfaces* **2021**, *13*, 40656–40663. [CrossRef]
159. Chen, B.; Wang, S.; Zhang, X.; Zhu, W.; Cao, Z.; Hao, F. Reducing the interfacial voltage loss in tin halides perovskite solar cells. *Chem. Eng. J.* **2022**, *445*, 136769. [CrossRef]

160. Shih, C.C.; Wu, C.G. Synergistic Engineering of the Conductivity and Surface Properties of PEDOT:PSS-Based HTLs for Inverted Tin Perovskite Solar Cells to Achieve Efficiency over 10. *ACS Appl. Mater. Interfaces* **2022**, *14*, 16125–16135. [CrossRef]
161. Cao, J.-J.; Lou, Y.-H.; Yang, W.-F.; Wang, K.-L.; Su, Z.-H.; Chen, J.; Chen, C.-H.; Dong, C.; Gao, X.-Y.; Wang, Z.-K. Multifunctional potassium thiocyanate interlayer for eco-friendly tin perovskite indoor and outdoor photovoltaics. *Chem. Eng. J.* **2022**, *433*, 133832. [CrossRef]
162. Zhang, Z.; Kamarudin, M.A.; Baranwal, A.K.; Wang, L.; Kapil, G.; Sahamir, S.R.; Sanehira, Y.; Chen, M.; Shen, Q.; Hayase, S. Indent-Free Vapor-Assisted Surface Passivation Strategy toward Tin Halide Perovskite Solar Cells. *ACS Appl. Mater. Interfaces* **2022**, *14*, 36200–36208. [CrossRef] [PubMed]
163. Wu, T.; Liu, X.; Luo, X.; Segawa, H.; Tong, G.; Zhang, Y.; Ono, L.K.; Qi, Y.; Han, L. Heterogeneous FASnI3 Absorber with Enhanced Electric Field for High-Performance Lead-Free Perovskite Solar Cells. *Nano-Micro Lett.* **2022**, *14*, 99. [CrossRef]
164. Zhou, J.; Hao, M.; Zhang, Y.; Ma, X.; Dong, J.; Lu, F.; Wang, J.; Wang, N.; Zhou, Y. Chemo-thermal surface dedoping for high-performance tin perovskite solar cells. *Matter* **2022**, *5*, 683–693. [CrossRef]
165. Wang, L.; Wang, Z.; Li, H.; Chang, B.; Pan, L.; Xie, Z.; Yin, L. Pseudohalide Anions to Suppress Oxidative Degradation for Efficient Formamidinium-Based Sn–Pb Halide Perovskite Solar Cells. *ACS Appl. Mater. Interfaces* **2022**, *14*, 18302–18312. [CrossRef] [PubMed]
166. Ghimire, N.; Bobba, R.S.; Gurung, A.; Reza, K.M.; Laskar, M.A.R.; Lamsal, B.S.; Emshadi, K.; Pathak, R.; Afroz, M.A.; Chowdhury, A.H.; et al. Mitigating Open-Circuit Voltage Loss in Pb–Sn Low-Bandgap Perovskite Solar Cells via Additive Engineering. *ACS Appl. Energy Mater.* **2021**, *4*, 1731–1742. [CrossRef]
167. Liu, H.; Sun, J.; Hu, H.; Li, Y.; Hu, B.; Xu, B.; Choy, W.C.H. Antioxidation and Energy-Level Alignment for Improving Efficiency and Stability of Hole Transport Layer-Free and Methylammonium-Free Tin-Lead Perovskite Solar Cells. *ACS Appl. Mater. Interfaces* **2021**, *13*, 45059–45067. [CrossRef] [PubMed]
168. Kim, H.; Lee, J.W.; Han, G.R.; Kim, S.K.; Oh, J.H. Synergistic Effects of Cation and Anion in an Ionic Imidazolium Tetrafluoroborate Additive for Improving the Efficiency and Stability of Half-Mixed Pb-Sn Perovskite Solar Cells. *Adv. Funct. Mater.* **2021**, *31*, 2008801. [CrossRef]
169. Jiang, T.; Xu, X.; Lan, Z.; Chen, Z.; Chen, X.; Liu, T.; Huang, S.; Yang, Y. Efficient MA-free Pb-Sn alloyed low-bandgap perovskite solar cells via surface passivation. *Nano Energy* **2022**, *101*, 107596. [CrossRef]
170. Hou, X.; Li, F.; Zhang, X.; Shi, Y.; Du, Y.; Gong, J.; Xiao, X.; Ren, S.; Zhao, X.-Z.; Tai, Q. Reducing the Energy Loss to Achieve High Open-circuit Voltage and Efficiency by Coordinating Energy-Level Matching in Sn–Pb Binary Perovskite Solar Cells. *Sol. RRL* **2021**, *5*, 2100287. [CrossRef]
171. Liu, H.; Wang, L.; Li, R.; Shi, B.; Wang, P.; Zhao, Y.; Zhang, X. Modulated Crystallization and Reduced VOC Deficit of Mixed Lead–Tin Perovskite Solar Cells with Antioxidant Caffeic Acid. *ACS Energy Lett.* **2021**, *6*, 2907–2916. [CrossRef]
172. Kim, H.; Lee, J.W.; Han, G.R.; Kim, Y.J.; Kim, S.H.; Kim, S.K.; Kwak, S.K.; Oh, J.H. Highly Efficient Hole Transport Layer-Free Low Bandgap Mixed Pb–Sn Perovskite Solar Cells Enabled by a Binary Additive System. *Adv. Funct. Mater.* **2022**, *32*, 2110069. [CrossRef]
173. Zhang, Z.; Liang, J.; Zheng, Y.; Wu, X.; Wang, J.; Huang, Y.; Yang, Y.; Zhou, Z.; Wang, L.; Kong, L.; et al. Balancing crystallization rate in a mixed Sn–Pb perovskite film for efficient and stable perovskite solar cells of more than 20% efficiency. *J. Mater. Chem. A* **2021**, *9*, 17830–17840. [CrossRef]
174. Zhang, L.; Kang, Q.; Song, Y.; Chi, D.; Huang, S.; He, G. Grain Boundary Passivation with Dion–Jacobson Phase Perovskites for High-Performance Pb–Sn Mixed Narrow-Bandgap Perovskite Solar Cells. *Sol. RRL* **2021**, *5*, 2000681. [CrossRef]
175. Zhang, K.; Späth, A.; Almora, O.; Le Corre, V.M.; Wortmann, J.; Zhang, J.; Xie, Z.; Barabash, A.; Hammer, M.S.; Heumüller, T.; et al. Suppressing Nonradiative Recombination in Lead–Tin Perovskite Solar Cells through Bulk and Surface Passivation to Reduce Open Circuit Voltage Losses. *ACS Energy Lett.* **2022**, *7*, 3235–3243. [CrossRef]
176. Sahamir, S.R.; Kamarudin, M.A.; Ripolles, T.S.; Baranwal, A.K.; Kapil, G.; Shen, Q.; Segawa, H.; Bisquert, J.; Hayase, S. Enhancing the Electronic Properties and Stability of High-Efficiency Tin–Lead Mixed Halide Perovskite Solar Cells via Doping Engineering. *J. Phys. Chem. Lett.* **2022**, *13*, 3130–3137. [CrossRef]
177. Li, Z.; Chang, Z.; Wang, K.; Bai, D.; Liu, L.; Yang, Y.; Wang, L.; Wang, S.; Liu, S. 4-Hydrazinobenzoic-Acid Antioxidant for High-Efficiency Sn–Pb Alloyed Perovskite Solar Cells. *Energy Technol.* **2022**, *10*, 2200217. [CrossRef]
178. Yu, Z.; Chen, X.; Harvey, S.P.; Ni, Z.; Chen, B.; Chen, S.; Yao, C.; Xiao, X.; Xu, S.; Yang, G.; et al. Gradient Doping in Sn–Pb Perovskites by Barium Ions for Efficient Single-Junction and Tandem Solar Cells. *Adv. Mater.* **2022**, *34*, 2110351. [CrossRef]
179. Guo, T.; Wang, H.; Han, W.; Zhang, J.; Wang, C.; Ma, T.; Zhang, Z.; Deng, Z.; Chen, D.; Xu, W.; et al. Designed p-type graphene quantum dots to heal interface charge transfer in Sn-Pb perovskite solar cells. *Nano Energy* **2022**, *98*, 107298. [CrossRef]
180. Peng, C.; Li, C.; Zhu, M.; Zhang, C.; Jiang, X.; Yin, H.; He, B.; Li, H.; Li, M.; So, S.K.; et al. Reducing Energy Disorder for Efficient and Stable Sn−Pb Alloyed Perovskite Solar Cells. *Angew. Chem.* **2022**, *134*, e202201209. [CrossRef]
181. Tong, J.; Jiang, Q.; Ferguson, A.J.; Palmstrom, A.F.; Wang, X.; Hao, J.; Dunfield, S.P.; Louks, A.E.; Harvey, S.P.; Li, C.; et al. Carrier control in Sn–Pb perovskites via 2D cation engineering for all-perovskite tandem solar cells with improved efficiency and stability. *Nat. Energy* **2022**, *7*, 642–651. [CrossRef]
182. Wang, J.; Yu, Z.; Astridge, D.D.; Ni, Z.; Zhao, L.; Chen, B.; Wang, M.; Zhou, Y.; Yang, G.; Dai, X.; et al. Carbazole-Based Hole Transport Polymer for Methylammonium-Free Tin–Lead Perovskite Solar Cells with Enhanced Efficiency and Stability. *ACS Energy Lett.* **2022**, *7*, 3353–3361. [CrossRef]

183. Kapil, G.; Bessho, T.; Sanehira, Y.; Sahamir, S.R.; Chen, M.; Baranwal, A.K.; Liu, D.; Sono, Y.; Hirotani, D.; Nomura, D.; et al. Tin–Lead Perovskite Solar Cells Fabricated on Hole Selective Monolayers. *ACS Energy Lett.* **2022**, *7*, 966–974. [CrossRef]
184. Shuaifeng, H.; Kento, O.; Richard, M.; Tomoya, N.; Minh Anh, T.; Takumi, Y.; Taketo, H.; Kazuhiro, M.; Kyohei, N.; Atsushi, S.; et al. Optimized Carrier Extraction at Interfaces for 23.6% Efficient Tin–Lead Perovskite Solar Cells. *Nat. Portf.* **2022**, *15*, 2096–2107. [CrossRef]